Geomorphology 300 (2018) 95–112

Contents lists available at ScienceDirect

Geomorphology

journal homepage: www.elsevier.com/locate/geomorph

Tracking morphological changes and slope instability using spaceborne and ground-based SAR data

Federico Di Traglia [a,*], Teresa Nolesini [a], Andrea Ciampalini [a], Lorenzo Solari [a], William Frodella [a], Fernando Bellotti [b], Alfio Fumagalli [b], Giuseppe De Rosa [a,c], Nicola Casagli [a]

[a] Dipartimento di Scienze della Terra, Università degli Studi di Firenze, Via La Pira 4, 50121 Firenze, Italy
[b] TRE ALTAMIRA srl, Ripa di Porta Ticinese, 79, 20143 Milano, Italy
[c] Il Vulcano a Piedi, Via Pizzillo, 98050, Stromboli, Italy

ARTICLE INFO

Article history:
Received 10 July 2017
Received in revised form 2 October 2017
Accepted 24 October 2017
Available online 26 October 2017

Keywords:
Volcano slope instability
SAR amplitude
SqueeSAR™
Ground-based InSAR

ABSTRACT

Stromboli (Aeolian Archipelago, Italy) is an active volcano that is frequently affected by moderate to large mass wasting, which has occasionally triggered tsunamis. With the aim of understanding the relationship between the geomorphologic evolution and slope instability of Stromboli, remote sensing information from space-born Synthetic Aperture Radar (SAR) change detection and interferometry (InSAR) () and Ground Based InSAR (GBInSAR) was compared with field observations and morphological analyses.

Ground reflectivity and SqueeSAR™ (an InSAR algorithm for surface deformation monitoring) displacement measurements from X-band COSMO-SkyMed satellites (CSK) were analysed together with displacement measurements from a permanent-sited, Ku-band GBInSAR system.

Remote sensing results were compared with a preliminary morphological analysis of the Sciara del Fuoco (SdF) steep volcanic flank, which was carried out using a high-resolution Digital Elevation Model (DEM). Finally, field observations, supported by infrared thermographic surveys (IRT), allowed the interpretation and validation of remote sensing data. The analysis of the entire dataset (collected between January 2010 and December 2014) covers a period characterized by a low intensity of Strombolian activity. This period was punctuated by the occurrence of lava overflows, occurring from the crater terrace evolving downslope toward SdF, and flank eruptions, such as the 2014 event.

The amplitude of the CSK images collected between February 22nd, 2010, and December 18th, 2014, highlights that during periods characterized by low-intensity Strombolian activity, the production of materials ejected from the crater terrace towards the SdF is generally low, and erosion is the prevailing process mainly affecting the central sector of the SdF. CSK-SqueeSAR™ and GBInSAR data allowed the identification of low displacements in the SdF, except for high displacement rates (up to 1.5 mm/h) that were measured following both lava delta formation after the 2007 eruption and the lava overflows of 2010 and 2011. After the emplacement of the 2014 lava field, high displacements in the central and northern portions of the SdF were recorded by the GBInSAR device, whereas the spaceborne data were unable to detect these rapid movements. A comparison between IRT images and GBInSAR-derived displacement maps acquired during the same time interval revealed that the observed displacements along the SdF were related to the crumbling of newly emplaced 2014 lava and of its external breccia. Detected slope instability after the 2014 flank eruption was related to lava accumulation on the SdF and to the difference in the material underlying the 2014 lava flow: i) lava flows and breccia layers related to the 2002–03 and 2007 lava flow fields in the northern SdF sector and ii) loose volcaniclastic deposits in the central part of the SdF. This work emphasizes the importance of smart integration of spaceborne, SAR-derived hazard information with permanent-sited, operational monitoring by GBInSAR devices to detect areas impacted by mass wasting and volcanic activity.

1. Introduction

The analysis of Synthetic Aperture Radar (SAR) images can provide several useful measurements, such as ground displacement, lithological and geomorphological changes, and topographic variations, which in turn can reveal insights regarding non-accessible, hazardous or poorly understood areas on a global scale (Massonnet and Feigl, 1995; Tizzani et al., 2009, 2015; Wadge et al., 2011; Ebmeier et al., 2012; Biggs et al., 2014; Pinel et al., 2014; Ciampalini et al., 2015; Del Ventisette et al., 2015; Arnold et al., 2016; Chaussard, 2017). Tracking lithological and geomorphological changes to the Earth's surface in

* Corresponding author.
E-mail address: federico.ditraglia@unifi.it (F. Di Traglia).

https://doi.org/10.1016/j.geomorph.2017.10.023

space and time is a crucial issue because of its practical use in damage assessment and disaster monitoring (Wadge et al., 2002, 2011; Stramondo et al., 2006; Saepuloh et al., 2010; Bignami et al., 2013; Solikhin et al., 2015; Frodella et al., 2016). Satellite SAR images are important resources for rapid mapping, particularly during post-event disaster scenarios, because their acquisition is not affected by the time of day or atmospheric conditions (Wadge et al., 2011). Moreover, the ability of SAR sensors to see through dense cloud cover facilitates hazard mitigation efforts during the crisis management of natural disasters (Wadge et al., 2011; Di Traglia et al., 2014a; Meyer et al., 2015; Calvari et al., 2016). SAR amplitude images can reveal newly formed deposits if their surfaces are sufficiently different from the underlying or surrounding materials, thus allowing the rapid mapping of areas impacted by earthquakes, tsunamis, landslides, floods, pyroclastic density currents, tephra falls and lava flows (Stramondo et al., 2006; Wadge et al., 2011). Tracking surface deformation using the phase difference between two SAR images (Differential SAR Interferometry, D-InSAR) was developed first for spaceborne applications (Massonnet and Feigl, 1998), and its use has been extended to ground-based microwave interferometer systems (Rudolf et al., 1999; Monserrat et al., 2014). Ground-Based InSAR (GBInSAR) systems were developed and implemented in the past two decades in order to allow nearly continuous observations of topographic changes and displacement measurements (Wadge et al., 2005), improving the understanding of volcanic activities, such as those at Soufrière Hills (Wadge et al., 2005, 2008, 2014), Arenal (Macfarlane et al., 2006), and Stromboli (Antonello et al., 2004; Tarchi et al., 2008; Di Traglia et al., 2014b, 2014c, 2015; Intrieri et al., 2013; Nolesini et al., 2013; Nolesini et al., 2013). Given their repeat time, GBInSARs led the InSAR technique from monitoring to surveillance and early-warning applications (Di Traglia et al., 2014a; Carlà et al., 2016a, 2016b; Frodella et al., 2017). Morphological analyses of volcanic areas are crucial for the identification of volcanic centres, tectonic structures, flow (lava, pyroclastic density currents or lahars) travel paths and emplacement areas and evidence of erosive processes (Bellotti et al., 2006; Cimarelli et al., 2013; Di Traglia et al., 2013, 2014d; Karátson et al., 2016). These studies benefitted enormously from the introduction of very high-resolution topography, such as Light Detection and Ranging Laser Imaging Detection and Ranging (LiDAR) and Terrestrial Laser Scanner (TLS) systems (Behncke et al., 2016; Jessop et al., 2012; Slatcher et al., 2015).

To constrain the geomorphologic evolution of the NW Stromboli unstable slope (SdF), in this work, the reflectivity (amplitude) of satellite SAR images that were collected by the X-band COSMO-SkyMed sensor was analysed. **S**lope instability phenomena at the Stromboli volcano in the period between January 2010 and December 2014 were detected by SqueeSAR™ analysis of the CSK dataset (CSK-SqueeSAR™) using a permanent-sited GBInSAR device (Di Traglia et al., 2014a). With the aim of obtaining morphometric features of the area, a preliminary morphological analysis was carried out using a 0.5 × 0.5 m resolution DEM. Field inspections that were also supported by infrared thermographic (IRT) surveys allowed the interpretation and validation of the remote sensing data. The acquired data cover a period characterized by low-intensity Strombolian activity, which is interrupted by stronger and frequent explosions, overflows from the crater terrace towards the SdF, and the 2014 flank eruption (Coppola et al., 2012; Calvari et al., 2014, 2016; Di Traglia et al., 2013, 2014a, 2014b, 2014c, 2015; Nolesini et al., 2013; Taddeucci et al., 2013; Zakšek et al., 2015).

2. Test site: Stromboli Island

Stromboli is a volcanic island in the Tyrrhenian Sea, off the northern coast of Sicily Island (southern Italy) (Fig. 1). The Stromboli volcano (926 m a.s.l.) is 2.6 km above the sea floor, is at the NE tip of the Aeolian archipelago, and belongs to a late Quaternary, large volcanic complex of mostly basalt to basaltic–andesitic composition (Tibaldi, 2001). The volcanic edifice was affected by three sector collapses, one of which occurred at 13 ka in the NW part of the volcanic edifice, producing the SdF depression (Tibaldi, 2001). Another large collapse event occurred at 5.6 ± 3.3 ka (Tibaldi, 2001), producing a massive landslide (0.73 ± 0.22 km^3, Di Roberto et al., 2010). Eruptive activity consists of the typical persistent, low-intensity Strombolian activity characterized by intermittent explosions from three vents (NE crater, NEC; SW crater, SWC; and central crater, CC) in the summit crater terrace (Blackburn et al., 1976; Calvari et al., 2014). This activity is often punctuated by periods dominated by stronger explosions and lava overflows from the crater terrace (Calvari et al., 2014; Di Traglia et al., 2013, 2014b, 2014c; Table 1) and/or by lava flows from ephemeral vents (flank eruptions) that occurred recently in 2002–03, 2007 and 2014 (Valade et al., 2016). Since the 2002–03 flank eruption and with improvement of the surveillance network, Stromboli has become one of the most monitored volcanoes in the world (Barberi et al., 2009). The 2002–03 flank eruption occurred on December 28th, 2002, after an intensification of the volcanic activity that began in November 2002 (Burton et al., 2008) with the opening of a NE-SW trending eruptive fissure that affected the NE vents from an elevation of approximately 750 m to 600 m a.s.l. (Table 1). Another flank eruption occurred on February 27th, 2007, with the opening of one ephemeral vent at 650 m a.s.l. at the base of the NE crater area, and a second ephemeral vent opened at 400 m a.s.l. within the SdF (Casagli et al., 2009). The 2007 flank eruption produced a lava delta, which extended down to 600 m below sea level within the SdF submarine slope area, with a total estimated volume of ≈7 × 10^6 m^3. In 2002, at the same location, a 9 × 10^6 m^3 mass of volcaniclastic material collapsed (Bosman et al., 2014). After the 2007 flank eruption ended (April 2nd, 2007; Calvari et al., 2014), several crises characterized by stronger explosions and lava overflows from the crater terrace occurred between September 2008 and May 2013 (Calvari et al., 2014; Di Traglia et al., 2014a). The last flank eruption started on August 7th, 2014, and lasted until November 13th, 2014, leading to the emplacement of a 7.4 × 10^6 m^3 lava field in the SdF, which developed from a fracture located at 650 m a.s.l. (Zakšek et al., 2015). The eruption was preceded by 2 months of increased Strombolian activity, characterized by several lava overflows from the craters, and variation of the monitoring parameters (Rizzo et al., 2015; Valade et al., 2016; Liotta et al., 2017), including the measurement of the displacement rate by the GBInSAR system (Di Traglia et al., 2015; Carlà et al., 2016a). The onset phase involved the breaching of the summit NE cone with the opening of an eruptive fissure on its northern flank, triggering a landslide along the SdF (Carlà et al., 2016b; Valade et al., 2016).

The SdF depression is filled with volcaniclastic deposits and lavas (Intrieri et al., 2013; Nolesini et al., 2013; Bonforte et al., 2016) emitted from a summit crater terrace at ≈750 m a.s.l. and from ephemeral vents within the SdF (Calvari et al., 2005). Following the classification proposed by Hungr et al. (2014), the slope instability phenomena at Stromboli are classified into three types (Di Traglia et al., 2017): 1) "*deep-seated gravitational slope deformations*" evolving in "*rock avalanches*" from the SdF, such as those recognized in the past history of Stromboli (volumes >10^7 m^3; Tibaldi, 2001); 2) "*rock* (*rotational or planar*) *slides*" evolving in "*rock avalanches*" from the SdF (volumes = 10^6–10^7 m^3; Bonaccorso et al., 2003; Tommasi et al., 2005; Tinti et al., 2006; Baldi et al., 2008); and 3) "*rock falls*" or "*gravel slides*" evolving in "*gravel flows*" (volumes <10^6 m^3), (Di Traglia et al., 2014a; Calvari et al., 2016). During the 2002–03 flank eruption, a type-2 landslide (25–30 × 10^6 m^3) occurred (Bonaccorso et al., 2003; Baldi et al., 2008). This phenomenon was triggered by the injection of a lateral sheet intrusion (Neri et al., 2008) and caused two tsunamis, which affected the coastline with a maximum run-up of 6–7 m at Stromboli village, causing minor structural damage and placing the local population at high risk (Tinti et al., 2006). During the 2007 and 2014 flank eruptions (February–April 2007, August–November 2014), the opening of ephemeral vents produced small type-3 landslides (Casagli et al., 2009; Carlà et al., 2016b). Periods dominated by stronger explosions

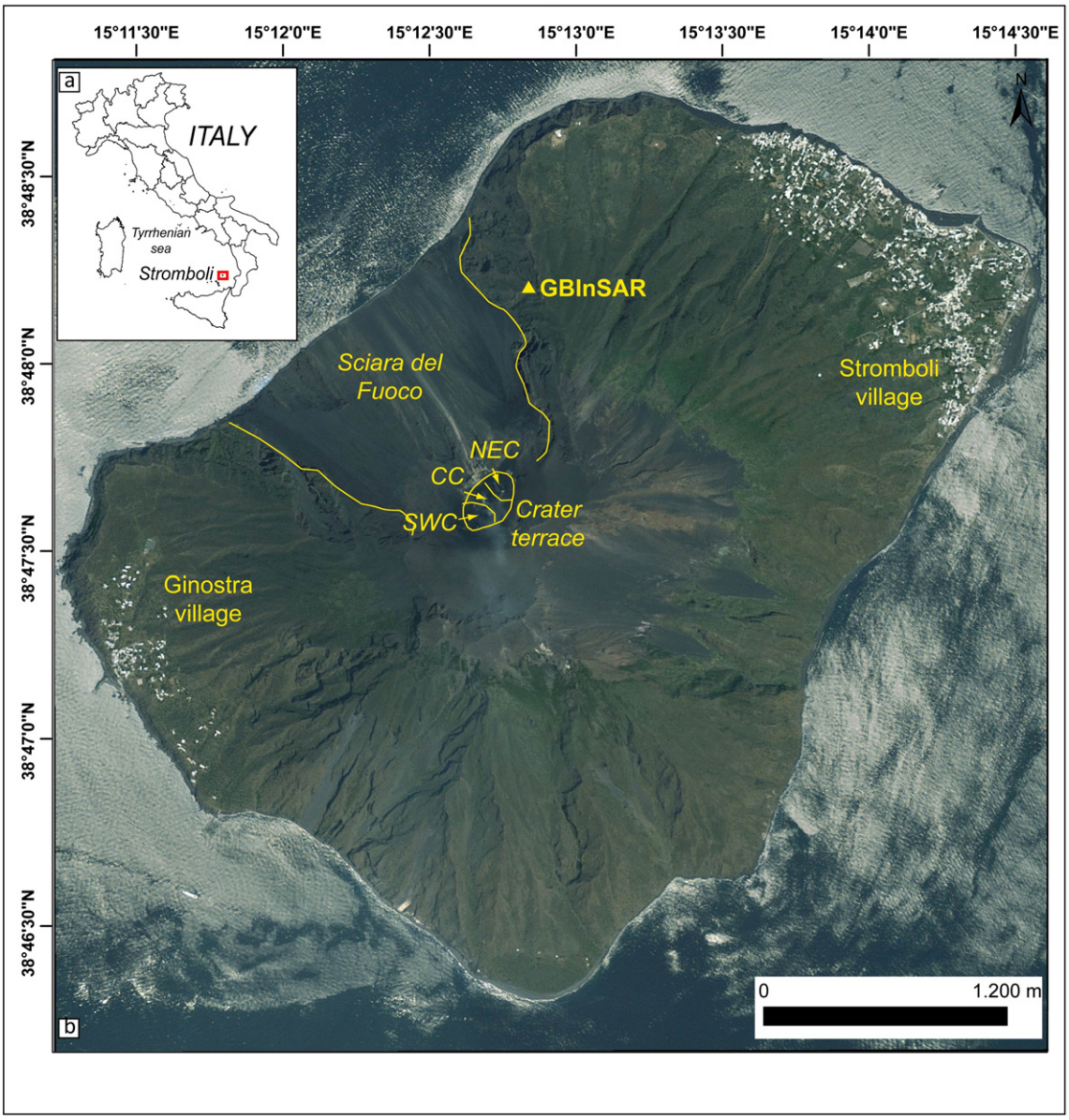

Fig. 1. a) Location of the island of Stromboli. b) The island of Stromboli. The Sciara del Fuoco (SdF), crater sectors and the location of the GBInSAR device are shown.

and lava overflows caused frequent gravel flows on the steep SdF slope (Di Traglia et al., 2014b; Calvari et al., 2016).

3. Methodological approach

3.1. Morphological analysis

A detailed morphometric analysis of the SdF was carried out using a high-resolution DEM with a spatial resolution of 50 cm (see Salvatici et al., 2016 for the DEM description). To derive the SdF terrain roughness map, any holes in the DEM were initially filled ("no data" pixels), and then, the Topographic Position Index (TPI; Guisan et al., 1999; Gallant and Wilson, 2000; Jenness, 2006) was calculated. TPI measures the relative topographic position of the central point as the difference between its elevation and the mean elevation within a defined neighbourhood (3 pixel radius) (De Reu et al., 2013).

The TPI was calculated using the focal operators and raster calculator of ESRI's ArcGIS 10.0 using the following equation:

$$TPI = (ELE - minELE)/(maxELE - minELE) \quad (1)$$

where *ELE* is the DEM-derived elevation and *minELE* and *maxELE* are the minimum and maximum elevation values, respectively. Both *minELE* and *maxELE* were calculated on a 3 × 3 pixel kernel window. Positive TPI values imply that the central point is located at a higher elevation than its average surroundings, while negative values denote a height lower than the average. The TPI depends on both elevation differences and the predetermined analysis radius/window (De Reu et al., 2013).

3.2. Detecting lithological and morphological changes by means of spaceborne SAR amplitude images

A dataset of 85 COSMO-SkyMed SAR (CSK) images acquired in descending orbit between February 22nd, 2010, and December 18th, 2014, was adopted for this study. The CSK images were collected in STRIPMAP - HIMAGE mode, achieving medium resolution, wide swath imaging and VV single polarization. The swath extension is ≥40 km, with a spatial resolution of 3 × 3 m single look, which is optimal for land-cover change detection (Covello et al., 2010; Bignami et al., 2013). The images were exploited as standard products, processing Level 1A - Single-Look Complex (SLC) slant products, with RAW data

Table 1
Summary of the eruptive activity at Stromboli volcano from 2010 to 2014.

Date	Eruptive activity	Slope instability	References
March 2010	Strong explosive event (March 10th, 2010), ejecta outside the crater, and rheomorphic lava flows to the NEC		Calvari et al. (2014)
May 2010–June 2010	Strong explosive events, rheomorphic lava flows and intracrateric lava flows		Calvari et al. (2014)
October 2010	Intracrater lava flow from the SWC vent (October 19th–26th, 2010)		Calvari et al. (2014)
December 2010–January 2011	Strong explosive events, intense spattering and overflows from the SWC		Coppola et al. (2012); Calvari et al. (2014)
March 2011	Strong explosive event (March 4th, 2011) from the SWC		Calvari et al. (2014)
June 2011–September 2011	Strong explosive events and two overflows	High displacement rate at SdF (August–October 2011)	Coppola et al. (2012); Calvari et al. (2014), Di Traglia et al. (2014a)
February–March 2012	Strong explosive events (February 15th–16th, 2012, March 6th, 2012)		Calvari et al. (2014); Di Traglia et al. (2014a)
July 2012–August 2012	Major explosions, intense spattering and overflows		Calvari et al. (2014)
December 2012–June 2013	Several lava overflows, strong explosive events and intense spatter activity, as well as a high displacement rate in the crater terrace	Crater-wall rock slide (January 12th, 2013), frequent rockfall and gravel flows during lava overflows	Calvari et al. (2014); Di Traglia et al. (2014a)
December 2013–March 2014	Strong explosive events, intense spattering, and anomalous degassing		Rizzo et al. (2015)
June 2014–November 2014	Several lava overflows, strong explosive events, landslides, intense spatter activity, opening of an ephemeral vent at 650 m a.s.l. (100 below the NEC), and lava flow lasting 3 months	Frequent rockfall and gravel flows during lava overflows and sliding of the NEC debris talus (August 7th, 2014)	Di Traglia et al. (2015); Rizzo et al. (2015); Zakšek et al. (2015)

focused in the slant range-azimuth projection, which is the sensor natural acquisition projection. The products also contain in-phase and quadrature of the focused data, which are weighted and radiometrically equalized (http://www.cosmo-skymed.it/docs/ASI-CSM-ENG-RS-092-A-CSKSARProductsHandbook.pdf). The products were co-registered using the offset refinement based on the Shuttle Radar Topography Mission (SRTM) DEM at 1 arc s, forming one unique stack that was cropped around the target area. The cropped stack was geocoded by correcting SAR geometric distortions using the SRTM DEM and producing the SAR orthorectified map-projected images. The backscattered intensity of each image, derived from real (i) and imaginary (q) parts of the complex SAR data, was transformed in the amplitude image and then decibel scaled, converting the data into a virtual band with the expression $10 * \log_{10}$ (amplitude). Finally, the quality of the images was enhanced using a multi-temporal speckle filter that reduces the salt-and-pepper-like texturing (speckle) of the CSK data (Dekker, 1998).

The radar echo for a given pixel depends on the coherent sum of the echoes from all scatterers within the corresponding resolution element (Wadge et al., 2002, 2011; Ebmeier et al., 2014; Pinel et al., 2014). Thus, the main factors determining the radar energy backscattered intensity from the radar antenna to the Earth's surface are as follows: i) local morphology, which in turn is relative to the radar look angle; ii) surface micro-relief (related to the grain-size) at the scale close to the radar wavelength; and iii) the dielectric constant of the material at the surface (Pinel et al., 2014). To define whether the micro-relief component of the roughness has strong backscattering properties, the Rayleigh criterion was applied to evaluate the root mean squared height (h_{rms}) variation on horizontal surfaces (Wadge et al., 2011) as follows:

$$h_{rms} > wavelenght/8\ cos(incidence\ angle) \quad (2)$$

For CSK images in descending orbit at Stromboli, h_{rms} is approximately 4 mm. Volcaniclastic deposits show a variation in the roughness of the surface: typically, deposits containing metre-sized blocks, smaller clasts and coarse tephra are "rough" to the radar, producing an increased backscatter, whereas fine-grained tephra are generally "smooth" to the radar (Wadge and Haynes, 1998; Wadge et al., 2002, 2011). Many lava surfaces have roughness, generating complex scattering processes (multiple scattering or backscatter enhancement) that are to be expected. However, the effects of the local morphology must also be considered. Surface irregularities having wavelengths at least twice as large as the satellite resolution cell cause signature variations from cell to cell due to changes in the local incidence angles (Dierking, 1999). Therefore, since it is not directly possible to separate the roughness effects due to factors such as the grain-size and morphology, the term "roughness" is used to represent a combination of both factors (Wadge et al., 2011).

To detect and interpret changes in land cover in connection with the SdF slope, two steps were applied in the employed procedure:

1) RGB colour composites and ratios (Wadge et al., 2002, 2011; Bignami et al., 2014), which is the simplest and the fastest approach when observing strong and homogeneous changes (Wadge et al., 2011; Bignami et al., 2014; Walter et al., 2015);
2) Texture analysis, using the GLCM (Grey Level Co-occurrence Matrix) method (Haralick et al., 1973), which is one of the most widely adopted techniques (e.g., Hussain et al., 2013; Pradhan et al., 2014; Whelley et al., 2014) for the derivation of these statistical methods.

Mathematically, the ratio is derived from the following:

$$I_r = [I_1(x,y)]/[I_2(x,y)] \quad (3)$$

where I_1 and I_2 are images from time t_1 and t_2, respectively, (x, y) are the coordinates of the pixel and I_r is the ratio image. Rignot and Zyl (1993) demonstrated that the image ratio depends on the relative average radar backscattering changes between two dates; these do not depend on the pixel's intensity level. Radiometric errors are usually introduced in the imagery during SAR processing (i.e., the computation of the scattering element size and/or the antenna pattern removal); these factors can be eliminated when computing the ratio image because calibration errors are exactly reproduced in repeat-pass imagery (Rignot and Zyl, 1993).

Among all the pattern elements used in the field of image interpretation, texture, which is a representation of the spatial relationship of the grey levels of the image, provides important characteristics for surface and object identification (Haralick et al., 1973; Pradhan et al., 2014). Texture characterization is made through second-order statistical measurements based on the GLCM and is used here as proposed by Haralick et al. (1973). Each entry (i, j) in the GLCM corresponds to the number of occurrences of the pair of grey levels i and j, which are a distance *d* apart in the original image (Haralick et al., 1973; Tonyé and Akono, 2002; Akono et al., 2006). The relative occurrence frequency of a pair of neighbouring pixels or resolution cells

having a distance d between them can be expressed as a matrix P_{ij}, called the GLCM. This symmetric matrix defines distance and direction, the so-called angular relationship of two neighbouring pixels, as a function (Haralick, 1979). Among the different features that can be derived from GLCM, only three are considered here: homogeneity, entropy, and the GLCM mean (Whelley et al., 2014). To improve and interpret the lithological and geomorphological variations in the SdF slope, GLCM features were combined in an RGB colour composite (Whelley et al., 2014; Table 2).

3.3. SqueeSAR™ displacement measurements

A range of processes associated with magmatic activity or structural instabilities can cause the deformation of a volcano's edifice, which is detectable with InSAR. Ground motion could be derived from the following: (i) magmatic inflation or deflation (e.g., Ruch et al., 2008; Tizzani et al., 2009, 2015), (ii) the thermal and mechanical contraction of lava fields (e.g., Ebmeier et al., 2012; Bato et al., 2016; Chaussard, 2016; Chen et al., 2017; Wittmann et al., 2017) or pyroclastic deposits (McAlpin et al., 2016), (iii) volcano slope instability (e.g., Ebmeier et al., 2010; Schaefer et al., 2015, 2016; Chen et al., 2017), (iv) dike intrusion (e.g., Bonforte and Guglielmino, 2015; González et al., 2015; Froger et al., 2015), and (v) edifice faulting and spreading (e.g., Froger et al., 2001; Bonforte et al., 2013; Kim et al., 2017). Displacements can be retrieved from SAR data using a variety of methods, the most accurate of which is the differential InSAR (D-InSAR), although this method only gives displacement in the line of sight (LOS) direction (Hu et al., 2014). The interferometric phase can be corrupted by noise (decorrelation) caused by the contributions from scatterers summing differently between SAR acquisitions. Signal decorrelation can be related to different factors (temporal and geometric decorrelation, volume scattering, atmospheric effects and processing errors), and it is estimated by calculation of the "coherence" (values in the range 0–1) between two acquisitions (Zebker et al., 1996). Displacements can be estimated more accurately by processing many images together rather than by the two-image approach, using Multi-Temporal InSAR (MT-InSAR) techniques (Ferretti et al., 2001; Berardino et al., 2002; Hooper, 2008, Hooper et al., 2012; Hu et al., 2014; Pinel et al., 2014; Casagli et al., 2017), including Persistent Scatterer InSAR (PSI, Ferretti et al., 2001). This time series algorithm targets pixels ("persistent scatterer", PS, sometimes referred to as a "permanent scatterer"; Ferretti et al., 2001) whose scattering properties remain consistent both in time and from variable look directions. If one scatterer returns significantly more energy than other scatterers within a resolution element, however, decorrelation is reduced. With the purpose of measuring ground displacement, in this work, the SqueeSAR™ method was used (Ferretti et al., 2011); this second-generation PSI technique searches targets from a radar imaging dataset that involves not only an identified consistent PS but also homogeneous, spatially distributed scatterers (DS) in its analysis. PS usually corresponds to man-made objects (e.g., buildings, linear structures, and rocky outcrops), while DS are typically identified by a homogeneous ground surface, uncultivated land, desert or debris-covered areas, and scattered outcrops. Therefore, an increased number of identified points on the ground results in increased confidence of the ground motion by identifying and "squeezing" all possible ground target information relating to acceptable coherent levels for estimated optimum phase values for the PSI analysis (Ferretti et al., 2011; Ciampalini et al., 2015; Lagios et al., 2013).

Table 2
Results of the GCLM texture analysis.

GLCM features	Interpretation
Homogeneity + GLCM Mean + Entropy	Fine-grained volcaniclastic deposits, 2014 late-lava flow field or erosion
GLCM Mean + Minor Entropy	Coarse-grained volcaniclastic deposits or 2014 early-lava flow field
Entropy + Minor GLCM Mean	Lava overflows

Table 3
Summary of the field surveys carried out at Stromboli.

Period	Activities
July–September 2011	Field inspection in the Sciara del Fuoco area
January 8th–9th, 2013	Field inspection in the Sciara del Fuoco area, thermal camera survey (9 January 2013)
January 13th–19th, 2013	Field inspection in the Sciara del Fuoco and crater terrace areas
May 10th–25th, 2013	Field inspection in the Sciara del Fuoco and crater terrace areas
February 12th–13th, 2014	Field inspection in the Sciara del Fuoco area
July 6th–7th, 2014	Field inspection in the Sciara del Fuoco area
July 23rd-24th, 2014	Field inspection in the Sciara del Fuoco area
August 8th, 2014–October 31st, 2014	Field inspection in the Sciara del Fuoco and crater terrace areas, thermal camera survey (28–29 August 2014)
December 13th–14th, 2014	Field inspection in the Sciara del Fuoco area

3.4. Ground-based interferometric SAR displacement measurements

The Stromboli GBInSAR system is in a stable area out of the SdF. The hardware consists of a continuous-wave step-frequency (CW-SF) radar that creates a synthetic aperture by moving the antennas along a horizontal straight rail 3.0 m long and at steps of 5 mm. Step-by-step, the microwave transmitter produces continuous waves at 1601 discrete frequency values, ranging from 17.0 to 17.1 GHz (average wavelength = 17.5 mm). The receiver acquires both the in-phase and the quadrature components of the microwave signal backscattered by the target. Range and cross-range synthesis of the complex images is obtained by coherently summing the signal contributions relative to different antenna positions and different microwave frequencies. As radar images are obtained through sampling techniques, frequency and spatial steps should be selected to avoid ambiguity in range and cross range (Rudolf et al., 1999; Tarchi et al., 2003a, 2003b, 2008). The Stromboli GBInSAR system produces a synthesized radar image of the observed area every 11 min, night and day, under any visibility condition, with a pixel resolution of approximately 2 m in range and 2 m on average in cross range and with a measured displacement precision lower than 1 mm. The system is installed within a cabinet, which is connected to an AC power supply line. Data transmission is provided by a HIPERLAN wireless antenna.

The displacement is calculated from the phase difference between the back-scattered microwave signals received at different times through the cross correlation between two SAR images. The cross correlation of the phase between two images taken at different times (T1 and T2) gives an interferogram showing, pixel by pixel, the phase difference produced in the time interval T2-T1. In the zero-baseline condition, this phase difference directly expresses the displacement that has occurred along the LOS in the time interval. Range and cross-range resolution are on average 2 × 2 m (Tarchi et al., 2003a, 2003b, 2008; Antonello et al., 2004; Casagli et al., 2009). The phase values can be affected by ambiguity (unwrapped

Table 4
FLIR sc620 thermal camera main technical specifications.

Feature	Unit	Value
Detector size	Pixel	640 × 480
Spectral range	μm	[7.5, 13]
Temperature range	°C	[−40, +500]
Thermal accuracy	°C	±2
Thermal sensitivity	mK	40
Field of view (F.O.V.)	Deg.	24 × 18
Spatial resolution	mrad	0.65
Minimum focus distance	m	0.3

phase), but due to the short elapsed time (11 min) between two subsequent measurements, the interferometric displacements are usually smaller than half the wavelength (in particular, 8.6 mm for the Ku-band); therefore, unwrapping procedures are generally not necessary (Antonello et al., 2004). Moreover, the latter is a time-consuming process, limiting the operational use of the GBInSAR during crisis management. For the GBInSAR images, a coherence mask (threshold equal to 0.8) is set to reduce the noisy areas of the interferogram (Luzi, 2010). The GBInSAR LOS allows the detection of the N—S components of the movements in all directions. Negative displacements (movements towards the sensor) represent inflation of the volcano crater area or inflation and sliding of the SdF, whereas positive displacements (movements away from the sensor) represent deflation of the crater area (Casagli et al., 2009; Di Traglia et al., 2013, 2014a, 2014b, 2014c, 2015) or instability of the internal rim of the crater terrace (Antonello et al., 2004).

Displacement maps and time-series are obtained by "stacking" the interferogram phase with a displacement measurement precision of 0.5 mm using (1 h to 8 h, depending on the observed displacement in the interferograms) averaged SAR images (Zebker et al., 1997; Antonello et al., 2004; Intrieri et al., 2013; Di Traglia et al., 2014c, 2015). GBInSAR time-series data were analysed in 7 × 7 pixel, large measurement areas (on average, 14 × 14 m). This approach is appropriate for the study of long time-series, highlighting persistent deformation and suppressing other random signals such as atmospheric anomalies (Hooper et al., 2012), especially when the deformation is episodic, with no change in source parameters over time (Pinel et al., 2014).

3.5. IRT surveys

Between 2011 and 2014, several multitemporal IRT surveys of the SdF were performed to analyse the volcaniclastic deposits and lava flow patterns, as well as the related impacted areas during the 2014 eruption (Table 3). The surveys, carried out by means of a handheld FLIR SC620 thermal camera (Table 4, FLIR, 2009), were performed as follows: i) on August 28th, 2014, on board a small Coast Guard vessel with an average distance of 800 m from the SdF coastline, visualizing the whole SdF scenario and ii) on September 3rd, approximately from the GBInSAR system location, from a mean distance of 500 m. To capture the whole SdF scenario, adjacent thermograms were mosaicked by means of FLIR Reporter 9 Professional (FLIR, 2012), whereas thermogram analyses were performed using FLIR ResearchIR 3.4 sp3 (FLIR, 2014). A built-in 3.2 M pixel digital camera, which acquires images in the visible range simultaneously with respect to the thermograms, allowed improvement of the detected thermal anomaly interpretation. (See Table 5.)

4. Data analysis

4.1. Morphology

The TPI was used to identify boundaries that may correspond to rock type or geomorphic processes. Large radius/window values primarily disclose major landscape units, while smaller values emphasize smaller topographic features. The generated TPI map (Fig. 2) highlights the presence of six different roughness-homogeneous areas within the SdF limit. Three areas are characterized by smooth surfaces (0.48 < TPI < 0.52), corresponding to the debris talus below the NEC and SWC and to the central portion of the SdF. The northern and western SdF are characterized by a complex morphology with the presence of ridges (TPI > 0.52) and depressions (TPI < 0.48) due to the presence of lava flows. Complex morphology also characterizes the crater terrace mainly due to the presence of scoria/spatter cones in the NEC, CC and SWC areas.

4.2. Change detection with CSK

CSK images, collected during low-intensity Strombolian activity, are characterized by changes in the backscattering in the central portion of the SdF, with a loss of the SAR amplitude between the two consecutive images (Fig. 3).

This area was also characterized by higher homogeneity and a lower GLCM mean and entropy (Fig. 4a; Table 2). During periods characterized by more frequent/intense Strombolian activity, lava overflows and the coarse-grained deposits emplaced by means of gravel flows produced lobes mainly located in the central part of the SdF (Fig. 4a, b, c). Gravel flow deposits are marked by the following: i) a strong increase in backscattering, ii) a decrease in the homogeneity. And iii) a contemporary increase in the entropy (Figs. 3, 4). Areas characterized by a decrease in SAR amplitude and by higher homogeneity correspond to the deposition of fine-grained material produced during gravel flow emplacement (Fig. 4b).

Using the two images collected before (July 27th, 2014) and after (August 12th, 2014) the onset of the 2014 effusive eruption (August 7th, 2014), changes were detected in the SdF northern sector, affected by a slight reduction in the backscattered amplitude (Fig. 3c, d). Alternating stripes of reduced and increased backscattering marked the central portion of the SdF. It is interesting to note that only a few parts of the SdF, marked by a reduction in SAR amplitude, were also affected by higher homogeneity, whereas almost the entire SdF was characterized by lower homogeneity and both a higher GLCM mean and entropy (Fig. 4d). The same image pair shows a strong reduction in the backscattering in conjunction with the NEC talus.

Images collected during the effusive phase (August 28th, 2014–November 16th, 2014) showed the occurrence of a large portion of decreasing SAR backscattering, located in a sector between the central and northern parts of the SdF (Fig. 3e, f). After the end of the effusive phase, this part showed a peculiar pattern of increased backscattering in the uphill portion and a decrease in the amplitude in the downhill part (Fig. 3g, h).

During the effusive phase, the feature identified using the RGB composition and amplitude ratio was characterized by high entropy and homogeneity in the texture analysis, while during the post-effusive phase, it was characterized by a strong increase in homogeneity. Moreover, the area characterized by high homogeneity increased downslope after the eruption ended (Fig. 4e, f).

Long-term analysis, carried out comparing the first (February 22nd, 2010) and the last images (December 18th, 2014) in the dataset, highlights areas characterized by morphological/lithological variations at a longer time scale (Fig. 5a). The area that suffered major changes is the central SdF, with evidence of erosion up-slope

Table 5
Peak LOS displacement rate registered in the Sciara del Fuoco during and after the 2014 flank eruption.

Date (dd/mm/yy)	Peak LOS disp. rate (mm/h)	Date (dd/mm/yy)	Peak LOS disp. rate (mm/h)	Date (dd/mm/yy)	Peak LOS disp. rate (mm/h)	Date (dd/mm/yy)	Peak LOS disp. rate (mm/h)
10/09/14	70	04/10/14	13	23/10/14	8.6	09/12/14	2.7
24/09/14	8.3	05/10/14	13	26/11/14	6.5	13/12/14	5
25/09/14	13.8	06/10/14	12.6	29/11/14	4.2	15/12/14	4.5
01/10/14	8	07/10/14	13	30/11/14	7	16/12/14	2.2
02/10/14	48	10/10/14	7.6	02/12/14	6.6		
03/10/14	13	19/10/14	12.9	05/12/14	1.6		

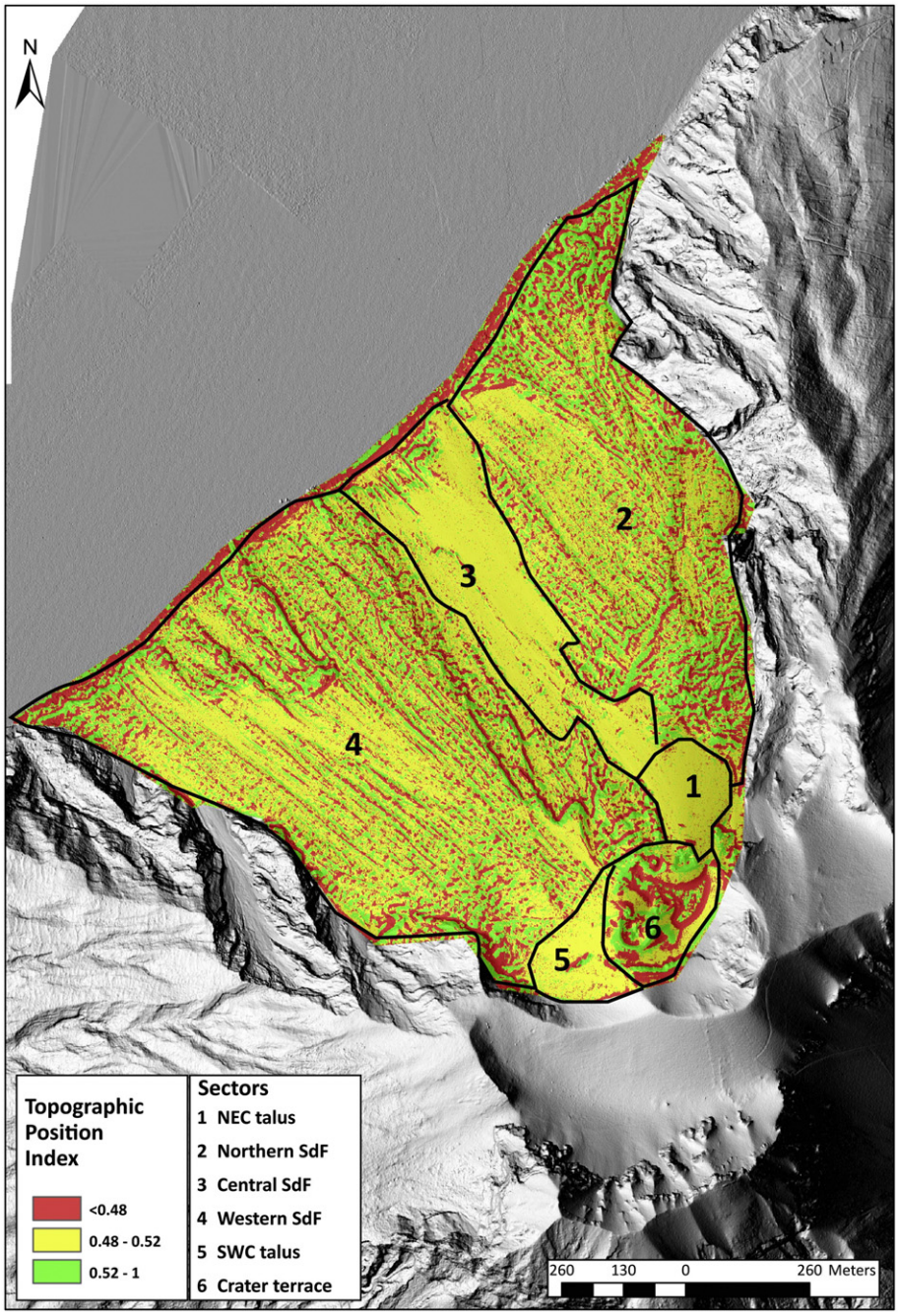

Fig. 2. SdF slope classification based on the TPI analysis. Six sectors were identified based on different roughness features.

and near-shoreline deposition. Larger variations are also recognizable near the 2014 vent, with the marked low amplitude ratio in the NEC talus area.

4.3. CSK-SqueeSAR™ displacement analysis

Ground displacement rates measured with CSK-SqueeSAR™ revealed the substantial stability of the SdF (0.1–0.5 mm/h), except for two anomalous areas (Figs. 5b, 6): i) the 2007 lava flow field and ii) the upper part of the western SdF, affected by the emplacement of overflows in December 2010 (Coppola et al., 2012; Calvari et al., 2014) and September 2011 (Coppola et al., 2012; Di Traglia et al., 2013; Calvari et al., 2014).

The latter area is characterized by a high displacement rate at the overflows (2.5 mm/h on average) and by an extensive area around them, with average displacement rates of 0.8 mm/h and a downslope decreasing trend. The 2007 lava flow field was studied, considering both the high slope gradient area and the lava delta. The former was characterized by a displacement rate on the order of 1.5 mm/h, whereas the lava delta showed differential ground motion, with the northern part being stable (0.1–0.5 mm/h) and with the central part characterized by a displacement rate on the order of 1.3 mm/h.

4.4. GBInSAR displacement analysis

During the period from January 1st, 2010–August 6th, 2014, the GBInSAR recorded slow ground displacement (<0.05 mm/h; see Di

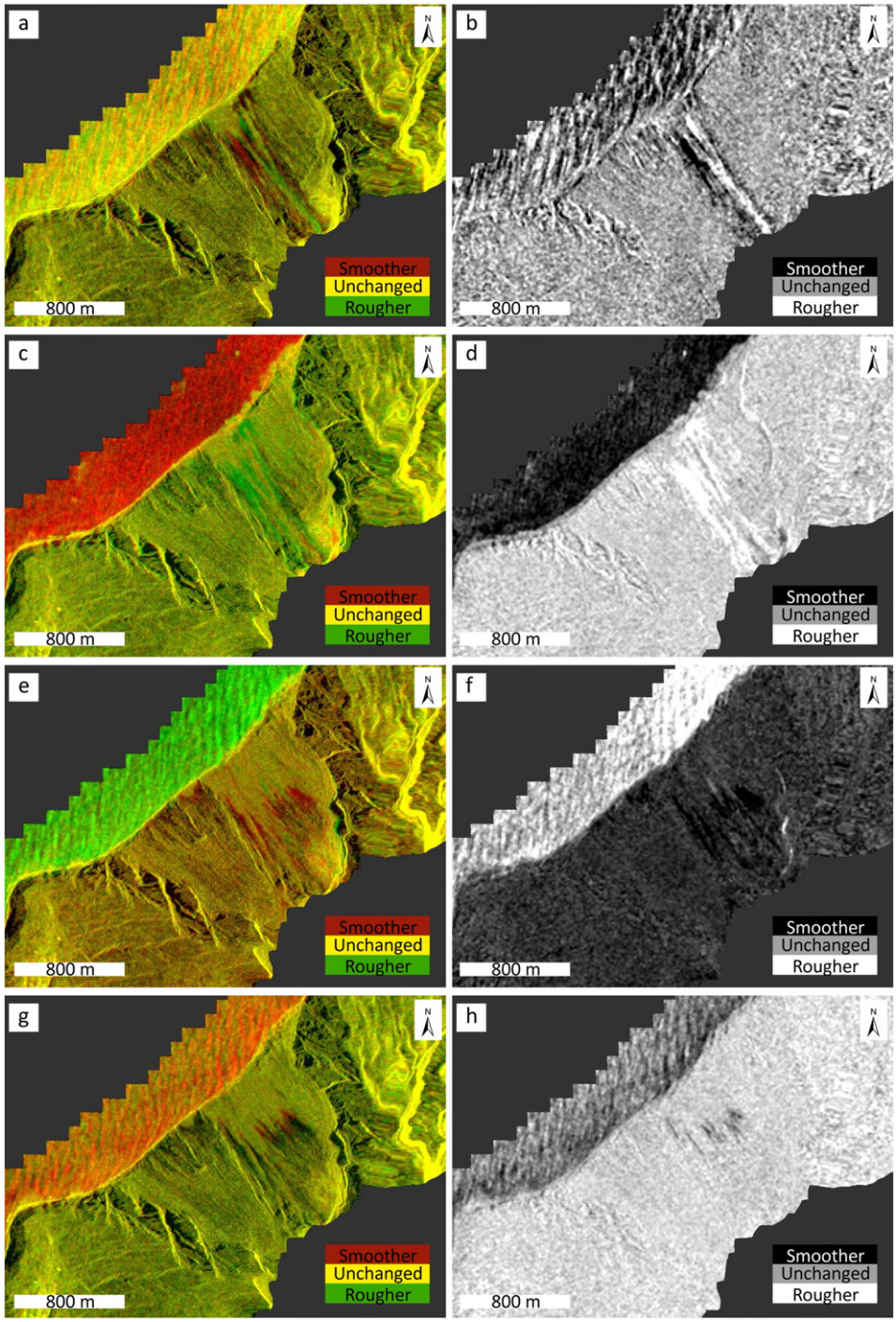

Fig. 3. CSK amplitude images (Left images: RGB colour composite; Right images: the amplitude ratio). a) and b) July 11th, 2014–July 27th, 2014; c) and d) July 27th, 2014–August 12th, 2014; e) and f) August 28th, 2014–November 16th, 2014; g) and h) November 16th, 2014–December 18th, 2014. In e) and f), the emplacement of the 2014 late-lava flows produced a decrease in the backscattering. The post-emplacement image comparison in g) and h) shows a slight increase in the backscattering in conjunction with the emplaced lava and an area characterized by the decrease in the SAR amplitude downslope.

Traglia et al., 2014a for threshold descriptions) in the SdF area (Figs. 7, 8). It is worth noting that the part of the SdF monitored by the GBInSAR device corresponds to the upper part of the northern SdF, as defined by the TPI. Since August 7th, 2014, after the onset of the 2014 flank eruption, the radar recorded a very low coherence in the SdF area (Fig. 7b) for three days; this was related to the initial fast-moving lava flow. Since August 10th, 2014, low coherence zones were related only to a small part of the monitored scenario, corresponding to active lava tongues, while the rest of the monitored SdF showed variable displacement rates (1–10 mm/h). After the end of the eruption (November 13th, 2014; Zakšek et al., 2015), the interferograms and cumulated maps derived from the GBInSAR data highlighted a complex displacement pattern within the SdF, with two different sectors characterized by slightly homogeneous displacement behaviour (Fig. 7a). In one sector (SdF1), in the central part of the area covered by the GBInSAR field of view (F.O.V.), the maximum total measured LOS displacement was 2757 mm towards the sensor (Figs. 7a, 8). From the single interferograms analysis, it was possible to detect fast movements in a

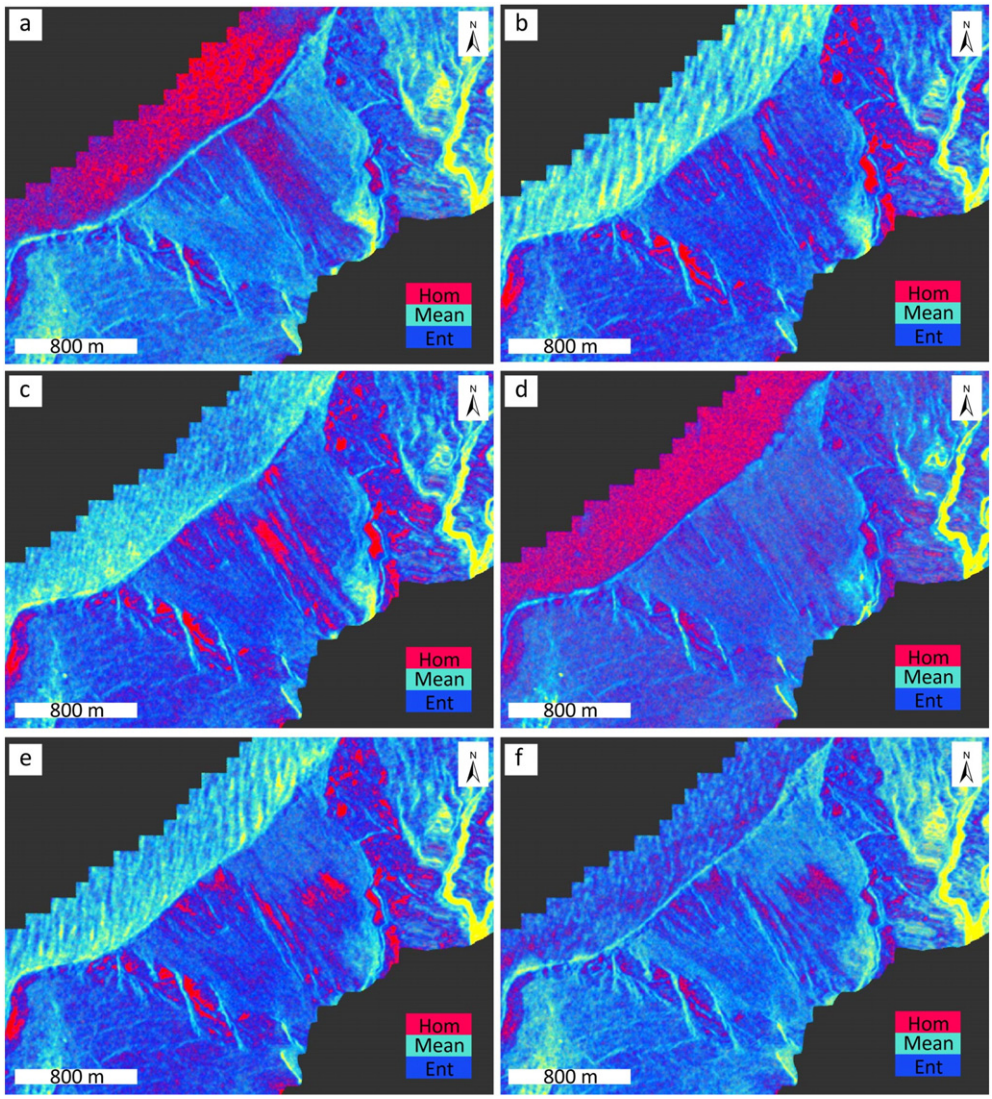

Fig. 4. RGB colour composite using GLCM features (RED: homogeneity; GREEN: mean; BLUE: entropy) derived from CSK amplitude images. a) May 8th, 2014; b) July 11th, 2014; c) July 27th, 2014; d) August 12th, 2014; e) November 16th, 2014; and f) December 18th, 2014. In e), the 2014 late-lava flows are characterized by higher entropy (BLUE channel) in the upper part and higher homogeneity (RED channel) in the lower part.

restricted portion within SdF1 (Fig. 7c). Fast movements occurred as short pulses (1–8 h time spans), with displacement peak rates up to 70 mm/h (Fig. 7c). Pulses occurred 22 times in the period between September 10th, 2014 (first pulse) until the end of the investigated period, with a progressive decrease in displacements and duration from the earlier pulse to the latter one (Table 3). The other sector (SdF2) is at a lower elevation near the northern border of the SdF. In this area, the maximum total recorded LOS displacement was 2362 mm towards the sensor (Fig. 7a).

4.5. IRT surveys

During periods characterized by frequent/intense Strombolian activity, as well as during the pre-2014 effusive phase, several lava overflows from the NEC area were observed and were always associated with rock falls that evolved into gravel flows along the SdF slope (Fig. 9a, b). Overflows produced dark lava tongues from the NEC area, whereas gravel flows produced deposition of coarse (cobble and boulders), dark materials along the shoreline and fine-grained, light grey materials on the SdF slope (Fig. 9e). On August 6th, 2014, gravel flows were associated with the sliding of the NEC hornito (Fig. 9c) and reached the sea, producing a small debris fan along the shoreline (Figs. 9e, 10c).

The lava flows emitted during the first week of the effusive phase reached the shoreline (≈1100 m from the vent at 650 m a.s.l.), covering the 2007 lava delta (Figs. 9d, e, 10c, d, e), whereas flows emitted later (August 14th–15th, 2014–November 13th, 2014) were characterized by a shorter travel distance due to a lower effusion rate (Zakšek et al., 2015; Valade et al., 2016), reaching only the upper part of the SdF slope (≈500–600 m from the vent; Figs. 9c, 10c). The late effusion formed two branches, one directed to the northern part of the SdF (Fig. 10b, c, e), and one channeling in the central part. These latter branches were mainly active in the final part of the effusion (October 2014), forming lobe-like morphologies in the central SdF (Figs. 9c, 10b, c, e).

Each lobe was characterized by a flow front and lateral levees that frequently fell, feeding gravel flows down the SdF to the sea. Comparison between thermograms (Fig. 11a) and GBInSAR-derived maps (Fig. 11b) acquired at the same time revealed that the observed displacement along the SdF was related to the movement along the slope of the newly emplaced lava and, in particular, of its external breccia. During late-lava effusion, rock falls from the crumbling of the newly emplaced lava, associated with the rolling of boulders along the SdF slope, were observed (Fig. 10d, e).

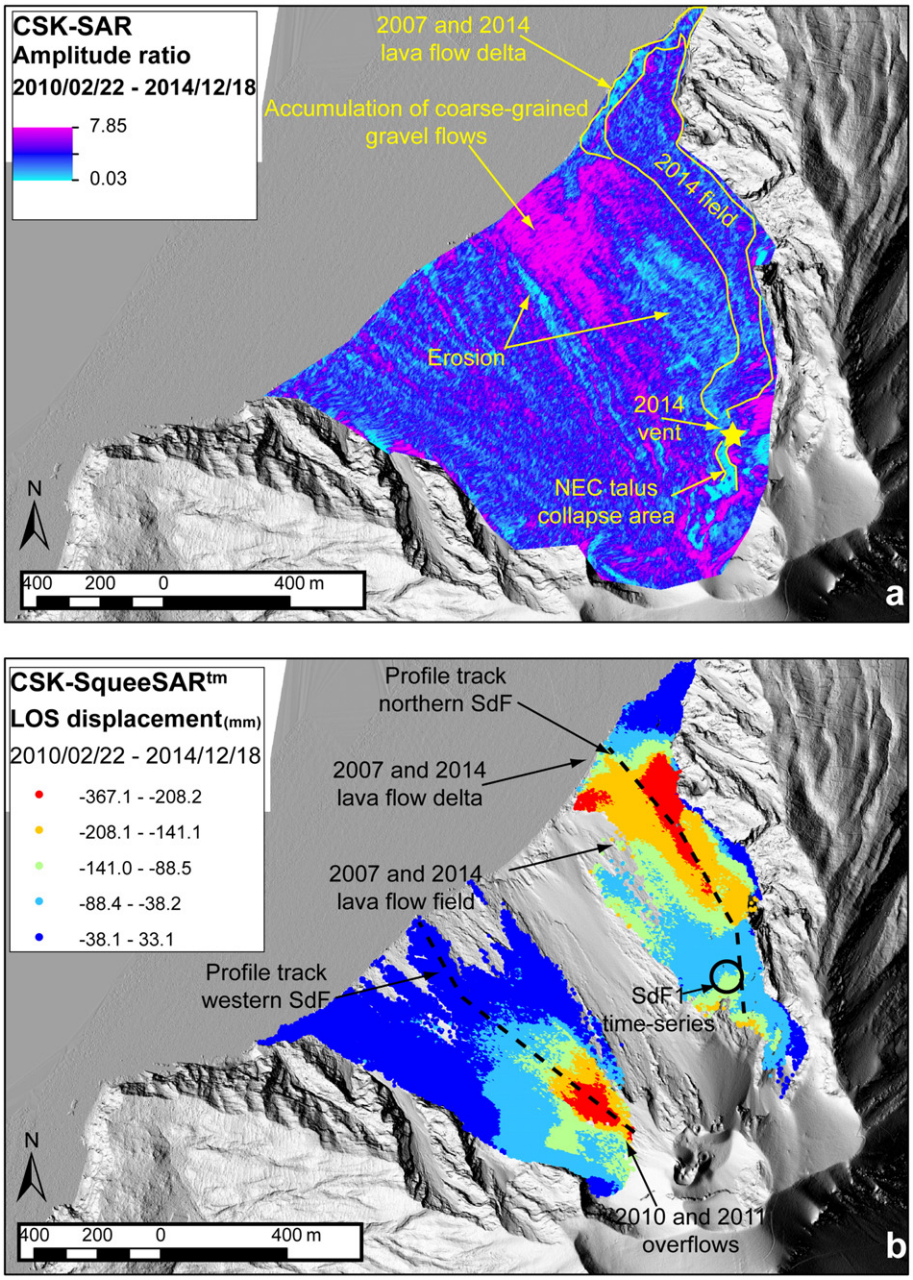

Fig. 5. Comparison between a) CSK amplitude image ratio and b) CSK-SqueeSAR™ LOS displacement maps (February 22nd, 2010–December 18th, 2014). Fig. 5a highlights the deposition in the central part of the SdF (high ratio), the change in the backscattering in the NEC debris talus area due to the landslide that occurred on August 7th, 2014, and the unchanged backscattering in the 2014 lava flow field due to the similar surface roughness between the newly emplaced lava flow and the previous surface (2007 lava flow). The area between the central and the northern portion of the SdF is characterized by a slight reduction in backscattering. This area corresponds to the late-lava flows emitted during the period of mid-August–early November 2014. In Fig. 5b, the maximum displacement recorded in the SdF sector is related to the presence of the 2007 and 2014 lava flows in the northern SdF and of the 2010 and 2011 overflows in the western SdF. The marked variation in the SAR backscattering in the central SdF is consistent with the accumulation of volcaniclastic material and produces a low coherence, making it impossible to measure displacements by means of the SqueeSAR™ technique.

5. Discussion

5.1. Geomorphological processes in the Sciara del Fuoco

At Stromboli, the central area of the SdF was characterized by processes that led to rapid and strong surface texture changes, such as erosion of volcaniclastic material, deposition of coarse-grained and fine-grained sediments, and lava emplacement. Fine-grained volcaniclastic materials are characterized by high homogeneity in the GLCM analysis possibly due to clast sorting (Whelley et al., 2014). Coarse-grained deposits related to dry gravel flows and lava flows are usually characterized by high entropy and GLCM means generated by boulders and external lava flow breccias (Whelley et al., 2014).

During low-intensity Strombolian activity, the production of materials ejected from the crater terrace to the SdF is generally low, and erosion is the prevailing process mainly affecting the central part of the SdF; the loss of backscattering between two consecutive images is a testament to this process (Table 6). Furthermore, this area is characterized by higher homogeneity and a lower GLCM mean and entropy possibly due to clast sorting and drainage organization within small colluvial fans in the central part of the SdF (Baldi et al., 2005, 2008).

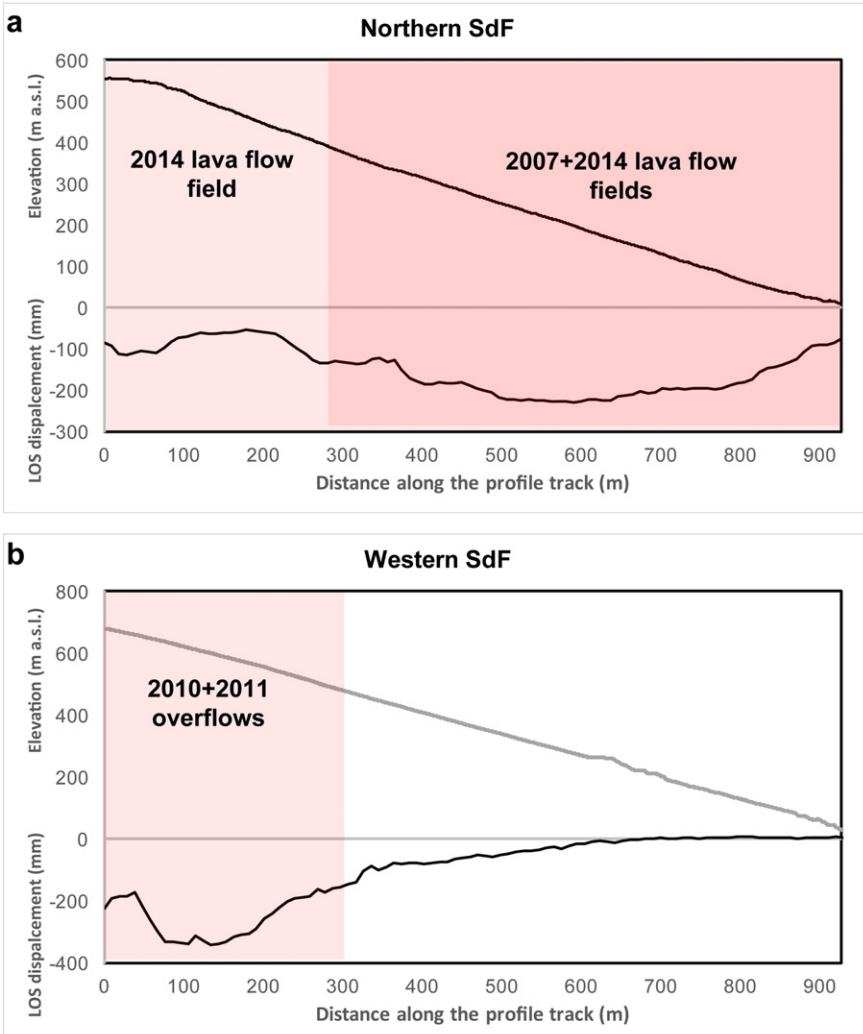

Fig. 6. Cumulative LOS displacement profiles along the a) northern SdF and b) western SdF. Profile tracks are shown in Fig. 5b.

The occurrence of frequent/intense Strombolian activity is marked by increases in backscattering, a testament to the deposition of coarser sediments and lava flows (Tables 4, 6). Positive amplitude differences and high ratios occurred with alternating stripes or lobes of reduced and increased backscattering and are mainly located in the central portion of the SdF. Areas of increased backscattering display a reduction in homogeneity, whereas decreases in the SAR amplitude correspond to higher homogeneity. Integration of SAR imagery with field and IRT data collected during the 2014 eruption provided the opportunity to interpret the increase in backscattering and reduction in homogeneity. These features are associated with lava overflow tongues from the crater terrace and/or cobbles and boulders emplaced by gravel flows associated with the sliding of crater walls/hornitos or by the crumbling of the lava overflows. On the other hand, areas of reduced SAR amplitude and high homogeneity correspond to the presence of fine-grained, light grey material on the SdF slope, related to ash clouds produced during the movement of gravel flows (Table 6).

Different lava flow behaviour was observed during the 2014 effusive and post-effusive eruption phase. Lava flows emplaced during the 2014 eruption early phases produced no remarkable changes in SAR backscattered amplitude probably due to the similar texture between the pre-effusive (2007 lava flows) and early lava flow surfaces (Fig. 5a). The 2007 lava flow and the early lava flow surfaces have high entropy and GLCM means because their surfaces are highly variable (such as lava with a blocky surface).

The marked reduction in the SAR backscattering and the high entropy and homogeneity observed between late August 2014 and the end of the eruption (Fig. 5a) correspond to a sector of strong erosion directly below an area characterized by the accumulation of a large amount of lava during the late 2014 eruption (Fig. 9e). The same area was characterized by a great increase in homogeneity downslope after the end of the eruption, together with a backscattering increase in the uphill SdF portion and an amplitude decrease in the downhill part. These features are consistent with the accumulation of volcaniclastic material produced during the eruption, due to the lava front and levee collapse, and after the effusion, due to external breccia remobilization (Lodato et al., 2007).

5.2. Slope instability of the Sciara del Fuoco

The high geomorphological dynamics in the SdF produced a large coherence loss in the CSK-SqueeSAR™ data, with less influence on the GBInSAR data (Fig. 5). Consequently, the SqueeSAR™ data are useful in only the northern and western parts of the SdF (Fig. 5b), while the GBInSAR system is monitoring only a portion of the northern part (Fig. 7). Major displacements in the SdF northern sector correspond with the 2014 lava flow fields. Different techniques of displacement measurements allowed the estimation of three dimensional displacements (e.g., Muller et al., 2015; Schaefer et al., 2017). In the case of only InSAR LOS measurements, the actual displacement vectors can be

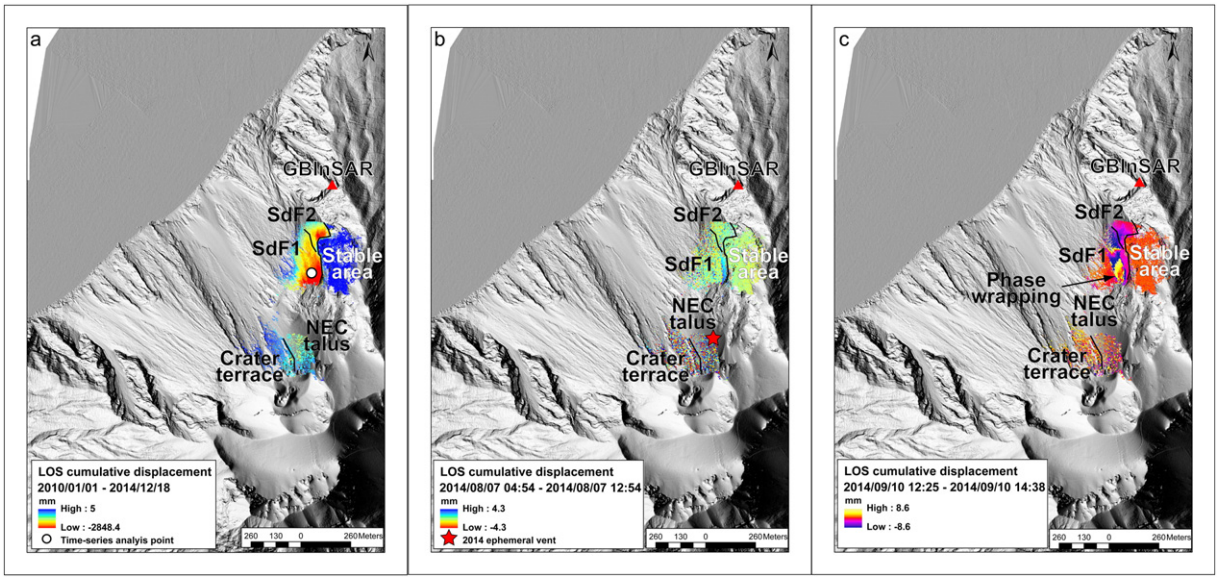

Fig. 7. a) Cumulative LOS displacement recorded by the GBInSAR during the interval of January 1st, 2010–December 14th, 2014; b) cumulative LOS displacement recorded by the GBInSAR during the period of August 7th, 2014–August 9th, 2014. The cumulative displacement map is strongly affected by temporal decorrelation due to rapid movements related to both the sliding of the NEC debris talus and the fast lava flows; c) GBInSAR interferogram formed using a pair of images recorded between 12:25 GMT and 14:38 GMT on September 10th, 2014 (first pulse recorded by the system). The interferogram is affected by phase wrapping. In the picture, the different sectors (crater terrace, debris talus, SdF1, and SdF2) are shown, as well as the position of the time-series analysis point. The images are overlain on a 0.5 × 0.5 m DEM-generated hill-shade image.

derived from the integration of three different sensors (Hu et al., 2014; Bardi et al., 2016). However, in the Stromboli case, the integration of the GBInSAR and CSK-SqueeSAR™ displacement vectors allows the estimation of the displacement in two dimensions (Fig. 8). Displacement vectors measured by the GBInSAR devices are directed towards the sensor, whereas the CSK-SqueeSAR™ displacement vectors are directed away from the satellites, and the vector reconstructed in two dimensions suggests a movement along the slope (Fig. 8). In the case of slow displacement rates, it would account for a general creep of the SdF, as suggested by Intrieri et al. (2013) and Nolesini et al. (2013).

GBInSAR and CSK-SqueeSAR™ displacement time series of the SdF1 area are compared in Fig. 8. In the case of the CSK-SqueeSAR™ displacement time series, areal averaging was applied (Fig. 5b). Despite the difference in the LOS direction, the two time series are fully comparable

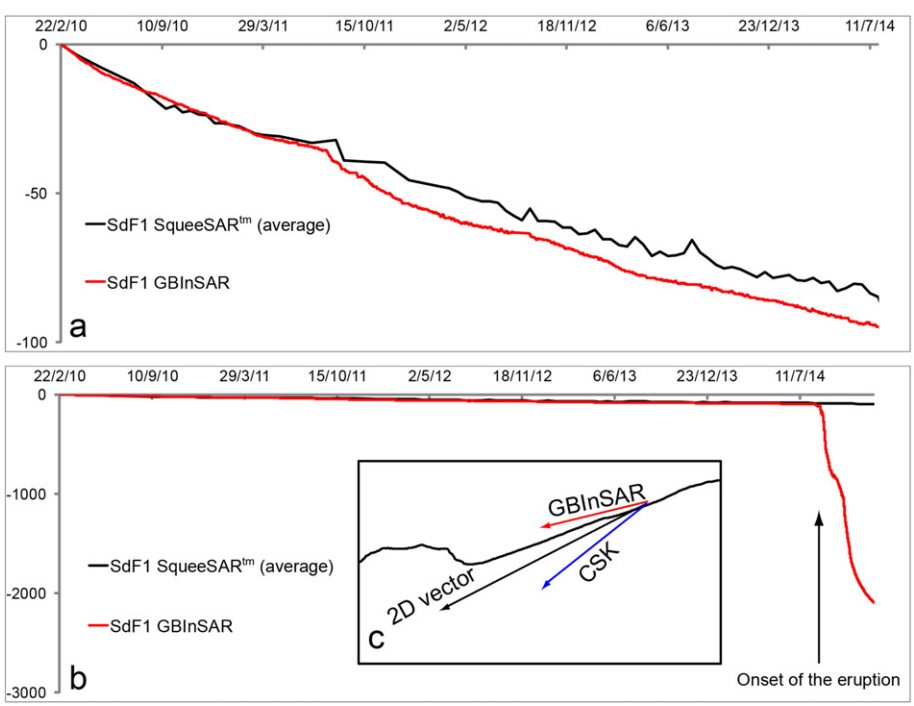

Fig. 8. SdF1 LOS displacement time-series measured by CSK-SqueeSAR™ and GBInSAR during the periods of a) February 22nd, 2010–July 27th, 2014, and b) February 22nd, 2010–December 18th, 2014. CSK-SqueeSAR™ measurement area is shown in Fig. 5b, while the GBInSAR measurement area is shown in Fig. 7a, c) difference in the LOS direction. The two time-series are fully comparable until the beginning of the 2014 eruption, while movements related to the newly emplaced lava flow field were properly detected by the GBInSAR device.

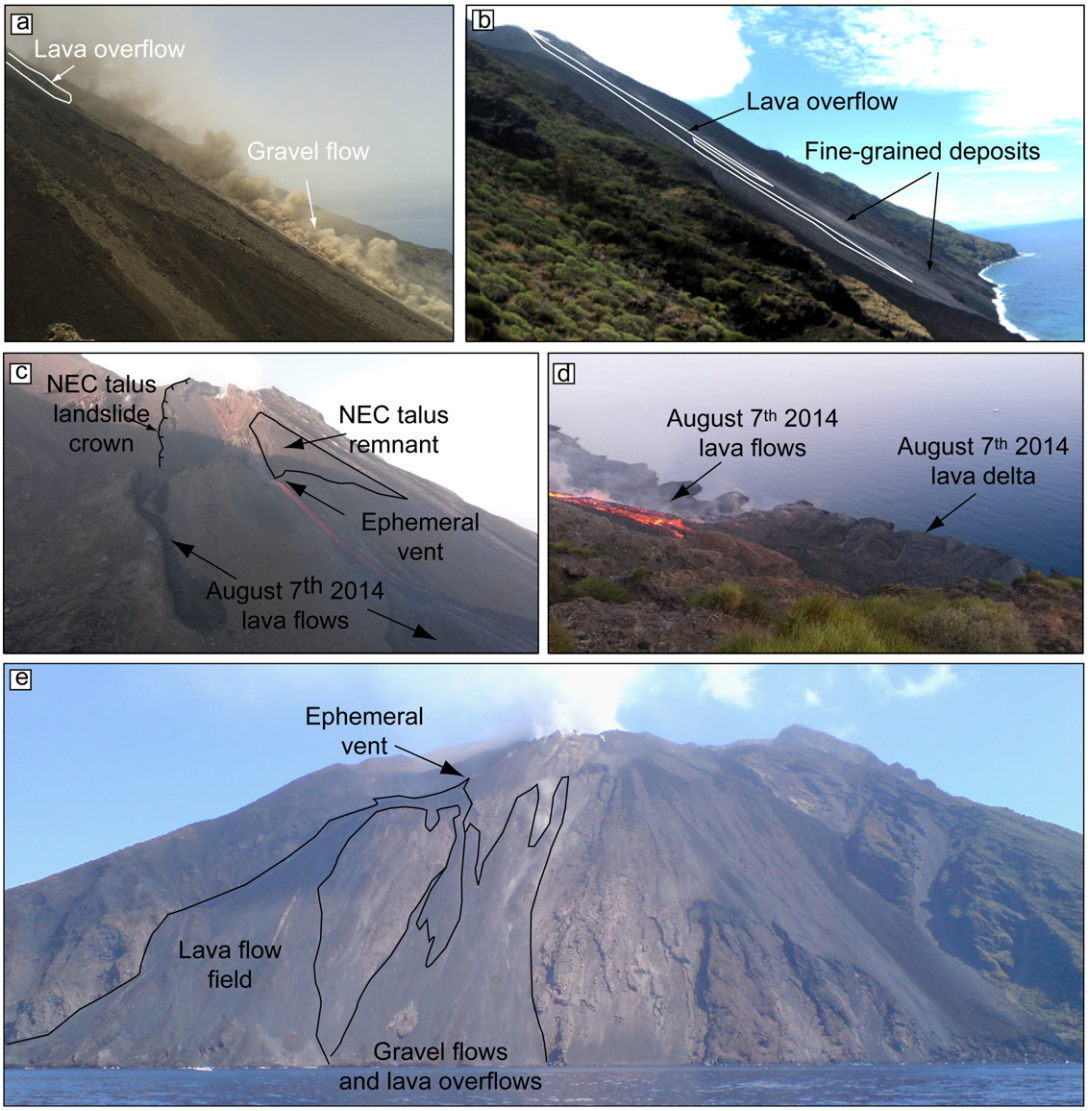

Fig. 9. a) Gravel flow along the SdF slope from a lava overflow (July 7th, 2014); b) lava overflow and fine-grained deposits derived from gravel flows along the SdF (July 24th, 2014); c) detail of the 2014 ephemeral vent area, highlighting the NEC talus landslide crown, the NEC talus remnant and the early-August lava flows (photo captured on August 8th, 2014, courtesy of G. De Rosa); d) the 2014 early-lava flows and the newly formed lava delta (photo captured on August 8th, 2014); e) SdF slope during the 2014 flank eruption (August 29th, 2014).

until the beginning of the 2014 eruption, and then, they diverge. This observation depends on different revisiting times between the GBInSAR and CSK satellites, which allowed GBInSAR to correctly measure the displacements, whereas the satellite was no longer able to follow the evolution of the deformation. InSAR data can detect post-emplacement lava flow movements due to four main components (Stevens et al., 2001; Dietterich et al., 2012; Ebmeier et al., 2012; Bagnardi et al., 2016; Bato et al., 2016; Chaussard, 2016): i) measurable subsidence of the flow surface due to thermal contraction; ii) time-dependent depression of the flow substrate; iii) movement of surface scatterers, resulting in radar phase decorrelation; and iv) slope instability due to overloading. The first two cases produce displacement vectors perpendicular to the slope with movements away from the sensor, whereas the slope instability phenomena are characterized by displacement vectors directed along the slope (Stevens et al., 2001). Moreover, the effect related to the latter case could be increased by thermal-induced fracturing of the lava flow. Although the estimation of the two main components of the movement is beyond the scope of this work, the reconstruction of the 2D vector integration of the GBInSARs and CSK LOS vectors has revealed that the movements during the 2014 flank eruption are primarily directed along the slope. Bonforte et al. (2016), analysing the SdF deformation after the 2002–03 flank eruption, revealed that thermal contraction is one of the dominant processes in only flat areas in the year following the lava emplacement, whereas slope movements characterized the SdF with a decreasing trend after the eruption. Further evidence to support this interpretation is derived from the displacement profile along the western SdF (Fig. 8c). Displacement related to the December 2010 and September 2011 overflows go far beyond the limits of the overflows themselves, accounting for general slope destabilization after the emplacement.

During the 2014 late-lava flow emplacement and after the effusion, GBInSAR data recorded large displacements in the SdF1 area, which are impossible to measure by means of the SqueeSAR™ technique applied to CSK imagery due to the satellite revisiting time (16 days during the 2014 flank eruption). In this area, the GBInSAR apparatus could catch fast movements that occurred as short pulses (Fig. 4c). The integration between GBInSAR and CSK amplitude images shows that the highest displacements are recorded in the area between the central and the

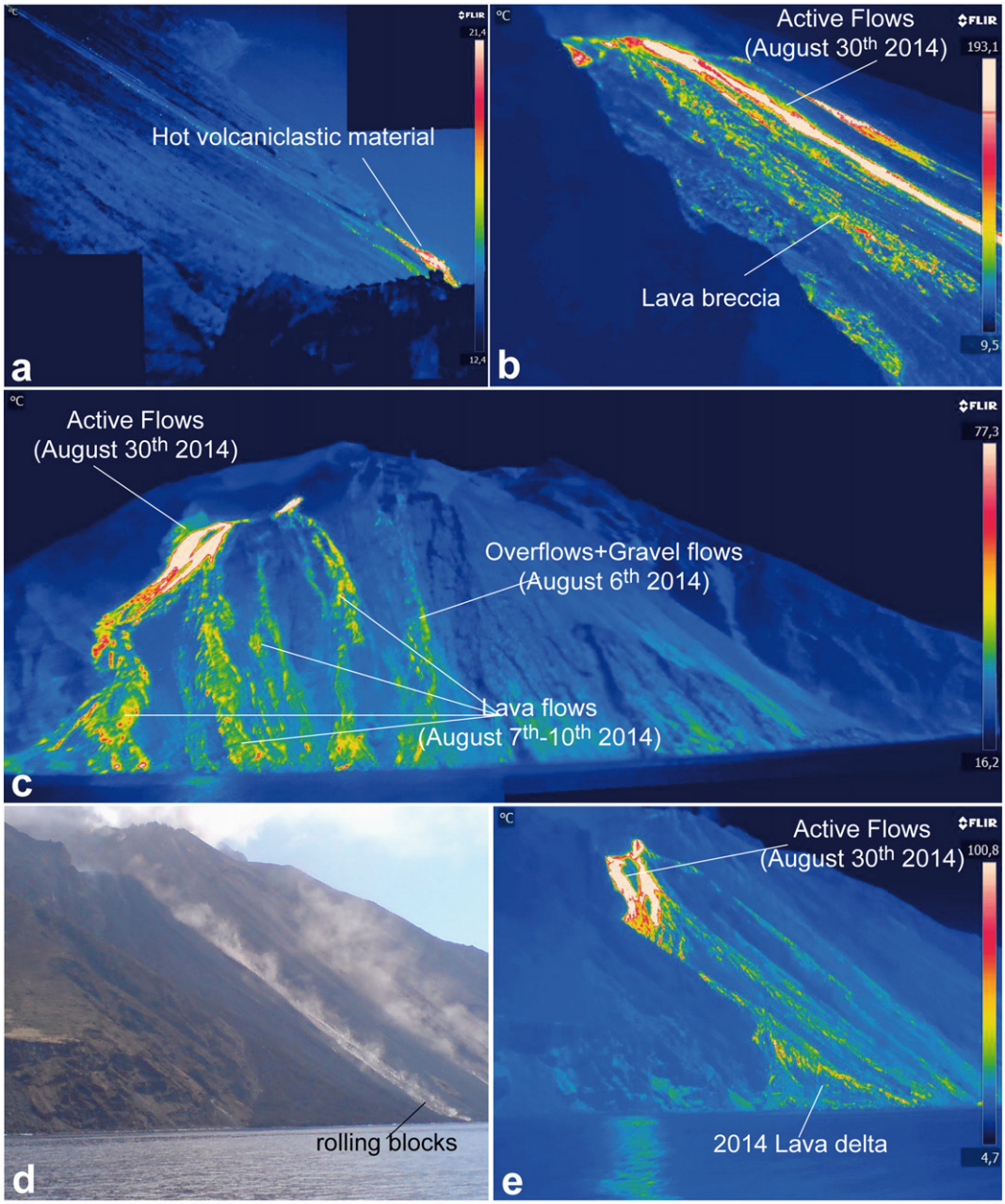

Fig. 10. Infrared thermographic surveys of the SdF. a) Mosaicked images (approximately 0.94 m pixel resolution) acquired on January 9th, 2013 (13:09 GMT), highlighting the accumulation of hot volcaniclastic material along the SdF shoreline during the 2012–13 frequent/intense Strombolian activity; b) single thermogram (approximately 0.57 m pixel resolution) acquired on September 3rd, 2014 (15:40 GMT), enhancing the 2014 late-lava flow (hotter parts) and its external breccia along the SdF northern sector (see Fig. 11 for details); c) mosaicked images acquired on August 29th, 2014 (15:14 GMT), visualizing the whole SdF area and highlighting the 2014 lava flow field (SdF northern sector) and the hot volcaniclastic material and lava overflow accumulation in the SdF central sector (approximately 0.67 m pixel resolution); d) single visible-light image acquired on August 29th, 2014 (15:19 GMT), showing rolling blocks on the SdF due to the 2014 lava crumbling and e) corresponding single thermogram (approximately 0.67 m pixel resolution) showing the active lava flows and the extension of the 2014 lava flow field and the newly formed lava delta, covering one that had formed during the 2007 flank eruption (Marsella et al., 2012).

northern SdF sectors, which are characterized by a decrease in SAR backscattering (Figs. 5, 7, 8). The lava accumulation on the SdF, the difference in the material below the newly emplaced lava between its northern and central parts, favoured the detected slope instability. The northern SdF part was characterized by lava flows and breccia layers (2002–03 and 2007 lava flows), whereas volcaniclastic loose deposits with minor lava lobes characterized the central part. At Stromboli, the inclination of the slopes exceeds the internal angle of friction of the volcaniclastic materials, but this condition is not sufficient to induce landslides (Nolesini et al., 2013). Analogue modeling by Nolesini et al. (2013) revealed that sliding processes are induced by the accumulation of either lava or spatter agglutinates, which produces an overloading effect, resulting in complex systems of landslides and an increasing volume of material involved in the sliding processes, as observed after the 2014 flank eruption.

6. Conclusions

In this work, SAR images were used to understand the relationship between geomorphologic evolution and slope instability at Stromboli volcano for the period between January 2010 and December 2014. Displacement data from a permanent-sited GBInSAR system were compared with the changes in the reflectivity (amplitude) of spaceborne SAR images collected by means of X-band

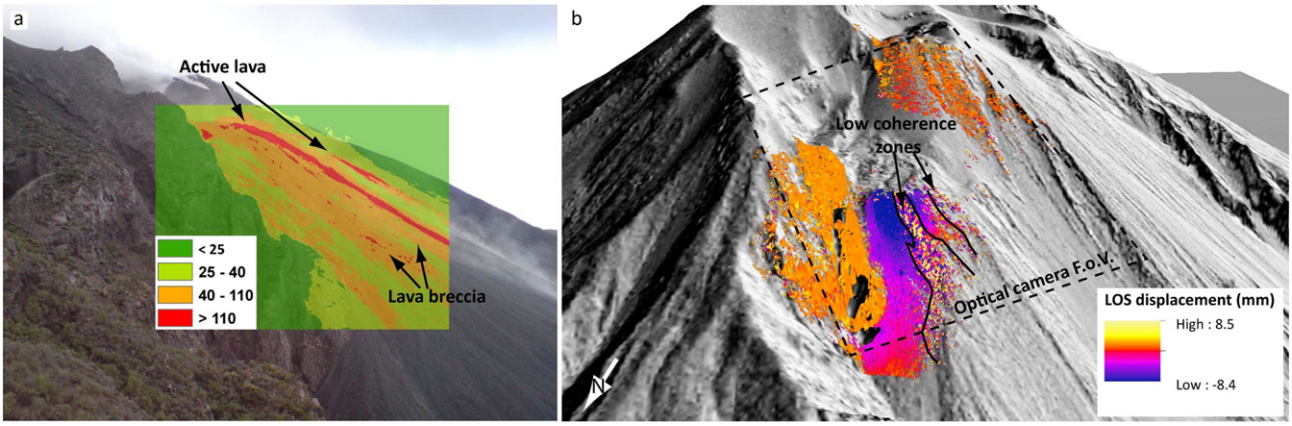

Fig. 11. Comparison between a) classified thermogram (September 3rd, 2014, 15:40 GMT) and b) GBInSAR LOS displacement map (September 3rd, 2014, 13:42–15.44 GMT), revealing that the detected displacement (blue coloured in b) was related to the slope instability of the newly emplaced lava (orange coloured in a). The active lava flows are marked by higher temperatures (red coloured in a) and decorrelation (salt-and-pepper texture in b).

Table 6
Features extracted by the analysis of the CSK amplitude data.

Date	SAR amplitude	GLCM	Interpretation
February 22nd, 2010–March 26th, 2010	Lobe below the NE crater in the eastern part of the SdF was defined by an increase in backscattering	Lobe with a clear decrease in homogeneity, associated with an increase in entropy	Accumulation of material related to a strong explosive event, associated with the emission of rheomorphic lava flows (Calvari et al., 2014)
March 26th, 2010–December 7th, 2010	Loss of backscattering in the central portion of the SdF between the two images	High homogeneity and low GLCM mean and entropy in the central portion of the SdF	Erosion in the central portion of the SdF
December 7th, 2010–December 23rd, 2010	Lobe below the SW crater, defined by an increase in backscattering	Lobe with a slight decrease in the homogeneity associated with the increase in entropy	Emission of a lava overflow from the SW crater (December 12th, 2010; Coppola et al., 2012; Calvari et al., 2014)
December 23rd, 2010–June 19th, 2011	Loss of backscattering in the central portion of the SdF between the two images	High homogeneity and low GLCM mean and entropy in the central portion of the SdF	Erosion in the central portion of the SdF
June 19th, 2011–August 6th, 2011	Lobe below the NE crater, in the northern part of the SdF, defined by an increase in backscattering	Lobe with a clear decrease in the homogeneity associated with the increase in entropy	Overflow from the NE crater along the SdF, related to the intense eruptive activity that occurred between June 2011 and September 2011 (Coppola et al., 2012; Di Traglia et al., 2013; Calvari et al., 2014, Di Traglia et al., 2014c)
August 6th, 2011-December 12th, 2012	Loss of backscattering in the central portion of the SdF between the two images	High homogeneity and low GLCM mean and entropy in the central portion of the SdF	Erosion in the central portion of the SdF
December 12th, 2012–December 28th, 2012	Alternating stripes of reduced and increased backscattering in the central portion of the SdF	Alternating stripes of high homogeneity and high entropy	Overflow from the NE crater (23–27 December 2012; Calvari et al., 2014; Di Traglia et al., 2014b)
December 28th, 2012–January 13th, 2013	Alternating stripes of reduced and increased backscattering in the central portion of the SdF and a reduction in backscattering in the debris talus below the NE crater	Alternating stripes of high homogeneity and high entropy	NE crater wall collapse and generation of rock avalanches along the SdF (January 12th, 2013; Di Traglia et al., 2014b), which are also highlighted by a strong decrease in homogeneity
January 13th, 2013–January 29th, 2013	Alternating stripes of reduced and increased backscattering in the central portion of the SdF	Alternating stripes of high homogeneity and high entropy	Overflow from the NE crater (January 14th–15th, 2013; Di Traglia et al., 2014b)
January 29th, 2013–June 9th, 2014	Loss of backscattering in the central portion of the SdF between the two images	High homogeneity and low GLCM mean and entropy in the central portion of the SdF	Erosion in the central portion of the SdF
June 9th, 2014–27th, July 2014	Strong increase in the whole central portion of the SdF, with lobes marked by decreased backscattering	Areas characterized by a backscattering increase display a reduction in homogeneity, while a loose SAR amplitude corresponds to higher homogeneity	Overflows and rock avalanches from the NE crater (Di Traglia et al., 2015)
July 27th, 2014–August 12th, 2014	Slight reduction in the backscattered amplitude in the northern sector of the SdF and increased backscattering in the central portion of the SdF	Almost the whole SdF was characterized by lower homogeneity and higher GLCM mean and entropy, while only few portions of the SdF marked by a reduction in SAR amplitude were also affected by higher homogeneity; the same image pairs show a strong reduction in backscattering in the debris talus located below the NE crater area	Overflows and rock avalanches from the NE crater, lava flow from the 650 m a.s.l. ephemeral vent, slide of the debris talus below the NE crater (Di Traglia et al., 2015; Carlà et al., 2016a, 2016b)
August 12th, 2014–November 16th, 2014	Decreasing SAR backscattering located between the central and northern parts of the SdF	High entropy and homogeneity	Late-lava flow from the 650 m a.s.l. ephemeral vent (Zakšek et al., 2015; Valade et al., 2016)
November 16th, 2014–December 18th, 2014	Increase in the backscattering uphill and a decrease in the amplitude in the downhill parts of the central and northern portions of the SdF	Homogeneity increases downslope	Downslope accumulation of the external breccia of the late-lava flows

COSMO-SkyMed satellites. Of the various spaceborne image analysis techniques, three were considered suitable for the analysis of amplitude images as a powerful tool for mapping areas affected by strong geomorphological changes: i) RGB colour composites using a SAR amplitude pair, ii) an amplitude ratio, and iii) GLCM texture analysis.

CSK-SqueeSAR™ and GBInSAR data allowed the identification of low displacements in the SdF, except for high displacement rates (up to 1.5 mm/h) measured following both the lava delta formation after the 2007 eruption and the lava overflows of 2010 and 2011. The integration of displacement data and the analysis of CSK amplitude images allowed us to identify the evolution of the slope instability phenomena and the geomorphological processes affecting the SdF slope. During periods characterized by low-intensity Strombolian activity, displacements within the SdF were low, and the CSK images showed backscattering and homogeneity values coherent with a phase of erosion of the volcanoclastic deposits of the central portion of the SdF. On the other hand, during the 2014 flank eruption, the SqueeSAR™ technique applied to the CSK imagery failed to catch actual displacement rates due to a long satellite revisiting time, while the GBInSAR apparatus recorded large displacements in the lava field area. The highest displacements are recorded in the area located between the central and the northern SdF sectors, which are characterized by a decrease in SAR backscattering. IRT surveys allowed analysis of the 2014 lava flow pattern evolution. The comparison between thermograms and GBInSAR accumulated maps revealed that the observed displacements along the SdF were related to the movement along the slope of the external breccias of the newly emplaced lava.

This work highlights the importance of a smart integration of spaceborne, SAR-derived hazard information into an operational monitoring environment (here, the permanent-sited GBInSAR), with the aim of detecting areas impacted by volcanic activity. The results presented here can be profitably generalized, adapted, modified, and updated in other geological contexts.

Acknowledgements

This work was financially supported by the “Presidenza del Consiglio dei Ministri – Dipartimento della Protezione Civile” (Presidency of the Council of Ministers - Department of Civil Protection) within the framework of the InGrID2015–2016 project; this publication, however, does not reflect the position and the official policies of the Department. This work was carried out using CSK® Products© ASI (Italian Space Agency), delivered under an ASI licence to use in the framework of COSMO-SkyMed Open Call for Science (Project Id: 191; Project title: Volcano InsTAbility – VITA; Scientific Coordinator: F. Di Traglia)”. The COSMO-SkyMed images were exploited from the COSMO-SkyMed data hub, managed by *E*-GEOS for ASI. The authors are grateful to E. Di Cuia (E-GEOS) for the technical support during the exploitation phase. F. Di Traglia has been supported by a post-doc fellowship founded by the “*Università degli Studi di Firenze – Ente Cassa di Risparmio di Firenze*” (D.R. n. 127804 (1206) 2015; “Volcano Sentinel” project). F. Di Traglia benefited from a post-doc mobility fellowship in “Geodesy and applied geophysics” by “Accademia dei Lincei - Royal Society” (Project title: “MOnitoring Volcano slope Instability - MOVIe”). X-band Cosmo-SkyMED images were processed using the freely delivered Sentinel Application Platform (SNAP) software. F. Di Traglia is grateful to R. Dal Naja and G. Marshall for inspiration.

Appendix A. Supplementary data

Supplementary data associated with this article can be found in the online version at doi:https://doi.org/10.1016/j.geomorph.2017.10.023. These data include the Google map of the most important areas described in this article.

References

Akono, A., Tankam, N.T., Tonye, E., Nyoungui, A.N., Dipanda, A., 2006. High order textural classification of two SAR ERS images on Mount Cameroon. Geocarto International 21 (3), 35–45.

Antonello, G., Casagli, N., Farina, P., Leva, D., Nico, G., Sieber, A.J., Tarchi, D., 2004. Ground-based SAR interferometry for monitoring mass movements. Landslides 1 (1), 21–28.

Arnold, D.W.D., Biggs, J., Wadge, G., Ebmeier, S.K., Odbert, H.M., Poland, M.P., 2016. Dome growth, collapse, and valley fill at Soufrière Hills Volcano, Montserrat, from 1995 to 2013: contributions from satellite radar measurements of topographic change. Geosphere 12 (4), 1300–1315.

Bagnardi, M., González, P.J., Hooper, A., 2016. High-resolution digital elevation model from tri-stereo Pleiades-1 satellite imagery for lava flow volume estimates at Fogo Volcano. Geophys. Res. Lett. 43 (12), 6267–6275.

Baldi, P., Fabris, M., Marsella, M., Monticelli, R., 2005. Monitoring the morphological evolution of the Sciara del Fuoco during the 2002–2003 Stromboli eruption using multi-temporal photogrammetry. ISPRS J. Photogramm. Remote Sens. 59 (4), 199–211.

Baldi, P., Coltelli, M., Fabris, M., Marsella, M., Tommasi, P., 2008. High precision photogrammetry for monitoring the evolution of the NW flank of Stromboli Volcano during and after the 2002–2003 eruption. Bull. Volcanol. 70 (6), 703–715.

Barberi, F., Civetta, L., Rosi, M., Scandone, R., 2009. Chronology of the 2007 eruption of Stromboli and the activity of the scientific synthesis group. J. Volcanol. Geotherm. Res. 182 (3), 123–130.

Bardi, F., Raspini, F., Ciampalini, A., Kristensen, L., Rouyet, L., Lauknes, T.R., Frauenfelder, R., Casagli, N., 2016. Space-borne and ground-based InSAR data integration: the Åknes test site. Remote Sens. 8 (3), 237.

Bato, M.G., Froger, J.L., Harris, A.J.L., Villeneuve, N., 2016. Monitoring an effusive eruption at Piton de la Fournaise using radar and thermal infrared remote sensing data: insights into the October 2010 eruption and its lava flows. Geol. Soc. Lond., Spec. Publ. 426 (1), 533–552.

Behncke, B., Fornaciai, A., Neri, M., Favalli, M., Ganci, G., Mazzarini, F., 2016. Lidar surveys reveal eruptive volumes and rates at Etna, 2007–2010. Geophys. Res. Lett. 43 (9), 4270–4278.

Bellotti, F., Capra, L., Groppelli, G., Norini, G., 2006. Tectonic evolution of the central-eastern sector of trans Mexican Volcanic Belt and its influence on the eruptive history of the Nevado de Toluca Volcano (Mexico). J. Volcanol. Geotherm. Res. 158 (1), 21–36.

Berardino, P., Fornaro, G., Lanari, R., Sansosti, E., 2002. A new algorithm for surface deformation monitoring based on small baseline differential SAR interferograms. IEEE Trans. Geosci. Remote Sens. 40 (11), 2375–2383.

Biggs, J., Ebmeier, S.K., Aspinall, W.P., Lu, Z., Pritchard, M.E., Sparks, R.S.J., Mather, T.A., 2014. Global link between deformation and volcanic eruption quantified by satellite imagery. Nat. Commun. 5.

Bignami, C., Ruch, J., Chini, M., Neri, M., Buongiorno, M.F., Hidayati, S., Sayudi, D.S., 2013. Pyroclastic density current volume estimation after the 2010 Merapi volcano eruption using X-band SAR. J. Volcanol. Geotherm. Res. 261, 236–243.

Bignami, C., Corradini, S., Merucci, L., De Michele, M., Raucoules, D., De Astis, G., Piedra, J., 2014. Multisensor satellite monitoring of the 2011 Puyehue-Cordon Caulle eruption. IEEE journal of selected topics in applied earth observations and remote sensing 7 (7), 2786–2796.

Blackburn, E.A., Wilson, L., Sparks, R.J., 1976. Mechanisms and dynamics of strombolian activity. J. Geol. Soc. 132 (4), 429–440.

Bonaccorso, A., Calvari, S., Garfì, G., Lodato, L., Patanè, D., 2003. Dynamics of the December 2002 flank failure and tsunami at Stromboli Volcano inferred by volcanological and geophysical observations. Geophys. Res. Lett. 30 (18).

Bonforte, A., Guglielmino, F., 2015. Very shallow dyke intrusion and potential slope failure imaged by ground deformation: the 28 December 2014 eruption on Mount Etna. Geophys. Res. Lett. 42 (8), 2727–2733.

Bonforte, A., Carnazzo, A., Gambino, S., Guglielmino, F., Obrizzo, F., Puglisi, G., 2013. A multidisciplinary study of an active fault crossing urban areas: the Trecastagni Fault at Mt. Etna (Italy). J. Volcanol. Geotherm. Res. 251, 41–49.

Bonforte, A., González, P.J., Fernández, J., 2016. Joint terrestrial and aerial measurements to study ground deformation: application to the Sciara del Fuoco at the Stromboli Volcano (Sicily). Remote Sens. 8 (6), 463.

Bosman, A., Casalbore, D., Romagnoli, C., Chiocci, F.L., 2014. Formation of an ‘a'ā lava delta: insights from time-lapse multibeam bathymetry and direct observations during the Stromboli 2007 eruption. Bull. Volcanol. 76 (7), 838.

Burton, M., Calvari, S., Spampinato, L., Lodato, L., Pino, N.A., Marchetti, E., Murè, F., 2008. Volcanic and seismic activity at Stromboli preceding the 2002–2003 flank eruption. The Stromboli Volcano: An Integrated Study of the 2002–2003 Eruption. AGU Geophysical Monograph Series 182, pp. 93–104.

Calvari, S., Spampinato, L., Lodato, L., Harris, A.J., Patrick, M.R., Dehn, J., Burton, M., Andronico, D., 2005. Chronology and complex volcanic processes during the 2002–2003 flank eruption at Stromboli Volcano (Italy) reconstructed from direct observations and surveys with a handheld thermal camera. J. Geophys. Res.: Solid Earth 110 (B2) 1978–2012.

Calvari, S., Bonaccorso, A., Madonia, P., Neri, M., Liuzzo, M., Salerno, G.G., Behncke, B., Caltabiano, T., Cristaldi, A., Giuffrida, G., La Spina, A., Marotta, E., Ricci, T., Spampinato, L., 2014. Major eruptive style changes induced by structural modifications of a shallow conduit system: the 2007–2012 Stromboli case. Bull. Volcanol. 76 (7), 1–15.

Calvari, S., Intrieri, E., Di Traglia, F., Bonaccorso, A., Casagli, N., Cristaldi, A., 2016. Monitoring crater-wall collapse at active volcanoes: a study of the 12 January 2013 event at Stromboli. Bull. Volcanol. 78, 1–16.

Carlà, T., Intrieri, E., Di Traglia, F., Casagli, N., 2016a. A statistical-based approach for determining the intensity of unrest phases at Stromboli volcano (Southern Italy) using one-step-ahead forecasts of displacement time series. Nat. Hazards 84 (1), 669–683.

Carlà, T., Intrieri, E., Di Traglia, F., Nolesini, T., Gigli, G., Casagli, N., 2016b. Guidelines on the use of inverse velocity method as a tool for setting alarm thresholds and forecasting landslides and structure collapses. Landslides:1–18 https://doi.org/10.1007/s10346-016-0731-5.

Casagli, N., Tibaldi, A., Merri, A., Del Ventisette, C., Apuani, T., Guerri, L., Fortuny-Guasch, J., Tarchi, D., 2009. Deformation of Stromboli Volcano (Italy) during the 2007 eruption revealed by radar interferometry, numerical modelling and structural geological field data. J. Volcanol. Geotherm. Res. 182 (3), 182–200.

Casagli, N., Frodella, W., Morelli, S., Tofani, V., Ciampalini, A., Intrieri, E., Raspini, F., Rossi, G., Tanteri, Lu, P., 2017. Spaceborne, UAV and ground-based remote sensing techniques for landslide mapping, monitoring and early warning. Geoenvironmental Disasters 4 (1), 9.

Chaussard, E., 2016. Subsidence in the Parícutin lava field: causes and implications for interpretation of deformation fields at volcanoes. J. Volcanol. Geotherm. Res. 320, 1–11.

Chaussard, E., 2017. A low-cost method applicable worldwide for remotely mapping lava dome growth. J. Volcanol. Geotherm. Res. 341:33–41. https://doi.org/10.1016/j.jvolgeores.2017.05.017.

Chen, Y., Remy, D., Froger, J.L., Peltier, A., Villeneuve, N., Darrozes, J., Perfettini, H., Bonvalot, S., 2017. Long-term ground displacement observations using InSAR and GNSS at Piton de la Fournaise volcano between 2009 and 2014. Remote Sens. Environ. 194, 230–247.

Ciampalini, A., Raspini, F., Bianchini, S., Frodella, W., Bardi, F., Lagomarsino, D., Di Traglia, F., Moretti, S., Proietti, C., Pagliara, P., Onori, R., Corazza, A., Duro, A., Basile, G., Casagli, N., 2015. Remote sensing as tool for development of landslide databases: the case of the Messina Province (Italy) geodatabase. Geomorphology 249, 103–118.

Cimarelli, C., Di Traglia, F., De Rita, D., Torrente, D.G., 2013. Space–time evolution of monogenetic volcanism in the mafic Garrotxa Volcanic Field (NE Iberian Peninsula). Bull. Volcanol. 75 (11), 758.

Coppola, D., Piscopo, D., Laiolo, M., Cigolini, C., Delle Donne, D., Ripepe, M., 2012. Radiative heat power at Stromboli Volcano during 2000–2011: twelve years of MODIS observations. J. Volcanol. Geotherm. Res. 215, 48–60.

Covello, F., Battazza, F., Coletta, A., Lopinto, E., Fiorentino, C., Pietranera, L., Valentini, G., Zoffoli, S., 2010. COSMO-SkyMed an existing opportunity for observing the earth. J. Geodyn. 49 (3), 171–180.

De Reu, J., Bourgeois, J., Bats, M., Zwertvaegher, A., Gelorini, V., De Smedt, P., Chu, W., Antrop, M., De Maeyer, P., Finke, P., Van Meirvenne, M., Verniers, J., Van Meirvenne, M., 2013. Application of the topographic position index to heterogeneous landscapes. Geomorphology 186, 39–49.

Dekker, R.J., 1998. Speckle filtering in satellite SAR change detection imagery. Int. J. Remote Sens. 19 (6), 1133–1146.

Del Ventisette, C., Solari, L., Raspini, F., Ciampalini, A., Di Traglia, F., Moscatelli, M., Pagliaroli, A., Moretti, S., 2015. Use of PSInSAR data to map highly compressible soil layers. Geol. Acta 13 (4), 309–323.

Di Roberto, A., Rosi, M., Bertagnini, A., Marani, M.P., Gamberi, F., 2010. Distal Turbidites and Tsunamigenic Landslides of Stromboli Volcano (Aeolian Islands, Italy). Submarine Mass Movements and their Consequences. Springer, Netherlands, pp. 719–731.

Di Traglia, F., Del Ventisette, C., Rosi, M., Mugnai, F., Intrieri, E., Moretti, S., Casagli, N., 2013. Ground-based InSAR reveals conduit pressurization pulses at Stromboli Volcano. Terra Nova 25 (3), 192–198.

Di Traglia, F., Morelli, S., Casagli, N., Monroy, V.H.G., 2014a. Semi-automatic delimitation of volcanic edifice boundaries: validation and application to the cinder cones of the Tancitaro–Nueva Italia region (Michoacán–Guanajuato Volcanic Field, Mexico). Geomorphology 219, 152–160.

Di Traglia, F., Nolesini, T., Intrieri, E., Mugnai, F., Leva, D., Rosi, M., Casagli, N., 2014b. Review of ten years of volcano deformations recorded by the ground-based InSAR monitoring system at Stromboli Volcano: a tool to mitigate volcano flank dynamics and intense volcanic activity. Earth Sci. Rev. 139, 317–335.

Di Traglia, F., Intrieri, E., Nolesini, T., Bardi, F., Del Ventisette, C., Ferrigno, F., Frangioni, S., Frodella, W., Gigli, G., Lotti, A., Tacconi Stefanelli, C., Tanteri, L., Leva, D., Casagli, N., 2014c. The ground-based InSAR monitoring system at Stromboli Volcano: linking changes in displacement rate and intensity of persistent volcanic activity. Bull. Volcanol. 76 (2), 1–18.

Di Traglia, F., Cauchie, L., Casagli, N., Saccorotti, G., 2014d. Decrypting geophysical signals at Stromboli Volcano (Italy): integration of seismic and ground-based InSAR displacement data. Geophys. Res. Lett. 41 (8), 2753–2761.

Di Traglia, F., Battaglia, M., Nolesini, T., Lagomarsino, D., Casagli, N., 2015. Shifts in the eruptive styles at Stromboli in 2010–2014 revealed by ground-based InSAR data. Sci Rep 5.

Di Traglia, F., Bartolini, S., Artesi, E., Nolesini, T., Ciampalini, A., Lagomarsino, D., Martí, J., Casagli, N., 2017. Susceptibility of intrusion-related landslides at volcanic islands: the Stromboli case study. Landslides 1–9.

Dierking, W., 1999. Quantitative roughness characterization of geological surfaces and implications for radar signature analysis. IEEE Trans. Geosci. Remote Sens. 37 (5), 2397–2412.

Dietterich, H.R., Poland, M.P., Schmidt, D.A., Cashman, K.V., Sherrod, D.R., Espinosa, A.T., 2012. Tracking lava flow emplacement on the east rift zone of Kīlauea, Hawai 'i, with synthetic aperture radar coherence. Geochem. Geophys. Geosyst. 13 (5).

Ebmeier, S.K., Biggs, J., Mather, T.A., Wadge, G., Amelung, F., 2010. Steady downslope movement on the western flank of Arenal volcano, Costa Rica. Geochem. Geophys. Geosyst. 11 (12), Q12004.

Ebmeier, S.K., Biggs, J., Mather, T.A., Elliott, J.R., Wadge, G., Amelung, F., 2012. Measuring large topographic change with InSAR: lava thicknesses, extrusion rate and subsidence rate at Santiaguito volcano, Guatemala. Earth Planet. Sci. Lett. 335, 216–225.

Ebmeier, S.K., Biggs, J., Muller, C., Avard, G., 2014. Thin-skinned mass-wasting responsible for widespread deformation at Arenal volcano. Front. Earth Sci. 2, 35.

Ferretti, A., Prati, C., Rocca, F., 2001. Permanent scatterers in SAR interferometry. IEEE Trans. Geosci. Remote Sens. 39 (1), 8–20.

Ferretti, A., Fumagalli, A., Novali, F., Prati, C., Rocca, F., Rucci, A., 2011. A new algorithm for processing interferometric data-stacks: SqueeSAR. IEEE Trans. Geosci. Remote Sens. 49 (9), 3460–3470.

FLIR, 2009. FLIR ThermaCAM SC620 Technical Specifications. http://www.flir.com/cs/emea/en/view/?id=41965.

FLIR (2012) FLIR Reporter Professional 9. http://www.flir.com/cs/emea/en/view/?id=42405.

FLIR (2014) FLIR ResearchIR 3.4. sp3 http://support.flir.com/DsDownload/Assets/T198206_en_40.pdf.

Frodella, W., Ciampalini, A., Gigli, G., Lombardi, L., Raspini, F., Nocentini, M., Scardigli, C., Casagli, N., 2016. Synergic use of satellite and ground based remote sensing methods for monitoring the San Leo rock cliff (northern Italy). Geomorphology 264, 80–94.

Frodella, W., Ciampalini, A., Bardi, F., Salvatici, T., Di Traglia, F., Basile, G., Casagli, N., 2017. A method for assessing and managing landslide residual hazard in urban areas. Landslides 1–15.

Froger, J.L., Merle, O., Briole, P., 2001. Active spreading and regional extension at Mount Etna imaged by SAR interferometry. Earth Planet. Sci. Lett. 187 (3), 245–258.

Froger, J.L., Famin, V., Cayol, V., Augier, A., Michon, L., Lénat, J.F., 2015. Time-dependent displacements during and after the April 2007 eruption of Piton de la Fournaise, revealed by interferometric data. J. Volcanol. Geotherm. Res. 296, 55–68.

Gallant, J.C., Wilson, J.P., 2000. Primary topographic attributes. In: Wilson, J.P., Gallant, J.C. (Eds.), Terrain Analysis: Principles and Applications. Wiley, New York, pp. 51–85.

González, P.J., Bagnardi, M., Hooper, A.J., Larsen, Y., Marinkovic, P., Samsonov, S.V., Wright, T.J., 2015. The 2014–2015 eruption of Fogo volcano: geodetic modeling of Sentinel-1 TOPS interferometry. Geophys. Res. Lett. 42 (21), 9239–9246.

Guisan, A., Weiss, S.B., Weiss, A.D., 1999. GLM versus CCA spatial modeling of plant species distribution. Plant Ecol. 143, 107–122.

Haralick, R.M., 1979. Statistical and structural approaches to texture. Proc. IEEE 67 (5), 786–804.

Haralick, R.M., Shanmugam, K., Dinstein, I.H., 1973. Textural features for image classification. Systems, Man and Cybernetics, IEEE Transactions on 6, 610–621.

Hooper, A., 2008. A multi-temporal InSAR method incorporating both persistent scatterer and small baseline approaches. Geophys. Res. Lett. 35 (16) (L16302).

Hooper, A., Bekaert, D., Spaans, K., Arıkan, M., 2012. Recent advances in SAR interferometry time series analysis for measuring crustal deformation. Tectonophysics 514, 1–13.

Hu, J., Li, Z.W., Ding, X.L., Zhu, J.J., Zhang, L., Sun, Q., 2014. Resolving three-dimensional surface displacements from InSAR measurements: a review. Earth Sci. Rev. 133, 1–17.

Hungr, O., Leroueil, S., Picarelli, L., 2014. The Varnes classification of landslide types, an update. Landslides 11 (2), 167–194.

Hussain, M., Chen, D., Cheng, A., Wei, H., Stanley, D., 2013. Change detection from remotely sensed images: from pixel-based to object-based approaches. ISPRS J. Photogramm. Remote Sens. 80, 91–106.

Intrieri, E., Di Traglia, F., Del Ventisette, C., Gigli, G., Mugnai, F., Luzi, G., Casagli, N., 2013. Flank instability of Stromboli Volcano (Aeolian Islands, southern Italy): integration of GB-InSAR and geomorphological observations. Geomorphology 201, 60–69.

Jenness, J. (2006). Topographic Position Index (tpi_jen. avx) Extension for ArcView 3. x, v. 1.3 a. Jenness Enterprises. URL: http://www.jennessent.com/arcview/tpi.htm.

Jessop, D.E., Kelfoun, K., Labazuy, P., Mangeney, A., Roche, O., Tillier, J.L., Trouillet, M., Thibault, G., 2012. LiDAR derived morphology of the 1993 Lascar pyroclastic flow deposits, and implication for flow dynamics and rheology. J. Volcanol. Geotherm. Res. 245, 81–97.

Karátson, D., Yepes, J., Favalli, M., Rodríguez-Peces, M.J., Fornaciai, A., 2016. Reconstructing eroded paleovolcanoes on Gran Canaria, Canary Islands, using advanced geomorphometry. Geomorphology 253, 123–134.

Kim, J.R., Lin, S.Y., Yun, H.W., Tsai, Y.L., Seo, H.J., Hong, S., Choi, Y., 2017. Investigation of potential volcanic risk from Mt. Baekdu by DInSAR time series analysis and atmospheric correction. Remote Sens. 9 (2), 138.

Lagios, E., Sakkas, V., Novali, F., Bellotti, F., Ferretti, A., Vlachou, K., Dietrich, V., 2013. SqueeSAR™ and GPS ground deformation monitoring of Santorini volcano (1992–2012): tectonic implications. Tectonophysics 594, 38–59.

Liotta, M., Rizzo, A.L., Barnes, J.D., D'Auria, L., Martelli, M., Bobrowski, N., Wittmer, J., 2017. Chlorine isotope composition of volcanic rocks and gases at Stromboli Volcano (Aeolian Islands, Italy): inferences on magmatic degassing prior to 2014 eruption. J. Volcanol. Geotherm. Res. 336, 168–178.

Lodato, L., Spampinato, L., Harris, A., Calvari, S., Dehn, J., Patrick, M., 2007. The morphology and evolution of the Stromboli 2002–2003 lava flow field: an example of a basaltic flow field emplaced on a steep slope. Bull. Volcanol. 69 (6), 661–679.

Luzi, G., 2010. Ground Based SAR Interferometry: A Novel Tool for Geoscience. INTECH Open Access Publisher.

Macfarlane, D.G., Wadge, G., Robertson, D.A., James, M.R., Pinkerton, H., 2006. Use of a portable topographic mapping millimetre wave radar at an active lava flow. Geophys. Res. Lett. 33 (3).

Marsella, M., Baldi, P., Coltelli, M., Fabris, M., 2012. The morphological evolution of the Sciara del Fuoco since 1868: reconstructing the effusive activity at Stromboli Volcano. Bull. Volcanol. 74 (1), 231–248.

Massonnet, D., Feigl, K.L., 1995. Discrimination of geophysical phenomena in satellite radar interferograms. Geophys. Res. Lett. 22 (12), 1537–1540.

Massonnet, D., Feigl, K.L., 1998. Radar interferometry and its application to changes in the Earth's surface. Rev. Geophys. 36 (4), 441–500.

McAlpin, D.B., Meyer, F.J., Gong, W., Beget, J.E., Webley, P.W., 2016. Pyroclastic flow deposits and InSAR: analysis of long-term subsidence at Augustine volcano, Alaska. Remote Sens. 9 (1), 4.

Meyer, F.J., McAlpin, D.B., Gong, W., Ajadi, O., Arko, S., Webley, P.W., Dehn, J., 2015. Integrating SAR and derived products into operational volcano monitoring and decision support systems. ISPRS J. Photogramm. Remote Sens. 100, 106–117.
Monserrat, O., Crosetto, M., Luzi, G., 2014. A review of ground-based SAR interferometry for deformation measurement. ISPRS J. Photogramm. Remote Sens. 93, 40–48.
Muller, C., del Potro, R., Biggs, J., Gottsmann, J., Ebmeier, S.K., Guillaume, S., Cattin, P.-H., Van der Laat, R., 2015. Integrated velocity field from ground and satellite geodetic techniques: application to Arenal volcano. Geophys. J. Int. 200 (2), 863–879.
Neri, M., Lanzafame, G., Acocella, V., 2008. Dyke emplacement and related hazard in volcanoes with sector collapse: the 2007 Stromboli (Italy) eruption. J. Geol. Soc. 165 (5), 883–886.
Nolesini, T., Di Traglia, F., Del Ventisette, C., Moretti, S., Casagli, N., 2013. Deformations and slope instability on Stromboli Volcano: integration of GBInSAR data and analog modeling. Geomorphology 180, 242–254.
Pinel, V., Poland, M.P., Hooper, A., 2014. Volcanology: lessons learned from synthetic aperture radar imagery. J. Volcanol. Geotherm. Res. 289, 81–113.
Pradhan, B., Hagemann, U., Tehrany, M.S., Prechtel, N., 2014. An easy to use ArcMap based texture analysis program for extraction of flooded areas from TerraSAR-X satellite image. Comput. Geosci. 63, 34–43.
Rignot, E.J., Van Zyl, J.J., 1993. Change detection techniques for ERS-1 SAR data. IEEE Trans. Geosci. Remote Sens. 31 (4), 896–906.
Rizzo, A.L., Federico, C., Inguaggiato, S., Sollami, A., Tantillo, M., Vita, F., Liuzzo, M., 2015. The 2014 effusive eruption at Stromboli Volcano (Italy): inferences from soil CO_2 flux and 3He/4He ratio in thermal waters. Geophys. Res. Lett. 42 (7), 2235–2243.
Ruch, J., Anderssohn, J., Walter, T.R., Motagh, M., 2008. Caldera-scale inflation of the Lazufre volcanic area, South America: evidence from InSAR. J. Volcanol. Geotherm. Res. 174 (4), 337–344.
Rudolf, H., Leva, D., Tarchi, D., Sieber, J., 1999. A mobile and versatile SAR system. Proc. Of IGARSS 1999. 28, pp. 592–594 28 June-2 July, Hamburg, Germany.
Saepuloh, A., Koike, K., Omura, M., Iguchi, M., Setiawan, A., 2010. SAR-and gravity change-based characterization of the distribution pattern of pyroclastic flow deposits at Mt. Merapi during the past 10 years. Bull. Volcanol. 72 (2), 221–232.
Salvatici, T., Di Roberto, A., Di Traglia, F., Bisson, M., Morelli, S., Fidolini, F., Bertagnini, A., Pompilio, M., Hungr, O., Casagli, N., 2016. From hot rocks to glowing avalanches: numerical modelling of gravity-induced pyroclastic density currents and hazard maps at the Stromboli Volcano (Italy). Geomorphology 273, 93–106.
Schaefer, L.N., Lu, Z., Oommen, T., 2015. Dramatic volcanic instability revealed by InSAR. Geology 43 (8), 743–746.
Schaefer, L.N., Lu, Z., Oommen, T., 2016. Post-eruption deformation processes measured using ALOS-1 and UAVSAR InSAR at Pacaya volcano, Guatemala. Remote Sens. 8 (1), 73.
Schaefer, L.N., Wang, T., Escobar-Wolf, R., Oommen, T., Lu, Z., Kim, J., Lundgren, P.R., Waite, G.P., 2017. Three-dimensional displacements of a large volcano flank movement during the May 2010 eruptions at Pacaya volcano, Guatemala. Geophys. Res. Lett. 44 (1), 135–142.
Slatcher, N., James, M.R., Calvari, S., Ganci, G., Browning, J., 2015. Quantifying effusion rates at active volcanoes through integrated time-lapse laser scanning and photography. Remote Sens. 7 (11), 14967–14987.
Solikhin, A., Pinel, V., Vandemeulebrouck, J., Thouret, J.C., Hendrasto, M., 2015. Mapping the 2010 Merapi pyroclastic deposits using dual-polarization Synthetic Aperture Radar (SAR) data. Remote Sens. Environ. 158, 180–192.
Stevens, N.F., Wadge, G., Williams, C.A., Morley, J.G., Muller, J.P., Murray, J.B., Upton, M., 2001. Surface movements of emplaced lava flows measured by synthetic aperture radar interferometry. J. Geophys. Res. Solid Earth 106 (B6), 11293–11313.
Stramondo, S., Bignami, C., Chini, M., Pierdicca, N., Tertulliani, A., 2006. Satellite radar and optical remote sensing for earthquake damage detection: results from different case studies. Int. J. Remote Sens. 27 (20), 4433–4447.
Taddeucci, J., Palladino, D.M., Sottili, G., Bernini, D., Andronico, D., Cristaldi, A., 2013. Linked frequency and intensity of persistent volcanic activity at Stromboli (Italy). Geophys. Res. Lett. 40 (13), 3384–3388.
Tarchi, D., Casagli, N., Moretti, S., Leva, D., Sieber, A.J., 2003a. Monitoring landslide displacements by using ground-based synthetic aperture radar interferometry: application to the Ruinon landslide in the Italian Alps. J. Geophys. Res. Solid Earth 108, B8.
Tarchi, D., Casagli, N., Fanti, R., Leva, D.D., Luzi, G., Pasuto, A., Pieraccini, M., Silvano, S., 2003b. Landslide monitoring by using ground-based SAR interferometry: an example of application to the Tessina landslide in Italy. Eng. Geol. 68 (1), 15–30.
Tarchi, D., Casagli, N., Fortuny-Guasch, J., Guerri, L., Antonello, G., Leva, D., 2008. Ground deformation from ground-based SAR interferometry. The Stromboli Volcano: An Integrated Study of the 2002–2003 Eruption. AGU Geophysical Monograph Series 182, pp. 359–372.
Tibaldi, A., 2001. Multiple sector collapses at Stromboli Volcano, Italy: how they work. Bull. Volcanol. 63 (2–3), 112–125.
Tinti, S., Pagnoni, G., Zaniboni, F., 2006. The landslides and tsunamis of the 30th of December 2002 in Stromboli analysed through numerical simulations. Bull. Volcanol. 68 (5), 462–479.
Tizzani, P., Battaglia, M., Zeni, G., Atzori, S., Berardino, P., Lanari, R., 2009. Uplift and magma intrusion at Long Valley caldera from InSAR and gravity measurements. Geology 37, 63–66.
Tizzani, P., Battaglia, M., Castaldo, R., Pepe, A., Zeni, G., Lanari, R., 2015. Magma amd fluid migration at Yellowstone Caldera in the last three decades inferred from InSAR, leveling, and gravity measurements. J. Geophys. Res. Solid Earth 120, 2627–2647.
Tommasi, P., Baldi, P., Chiocci, F.L., Coltelli, M., Marsella, M., Pompilio, M., Romagnoli, C., 2005. The landslide sequence induced by the 2002 eruption at Stromboli volcano. Landslides. Springer, Berlin Heidelberg, pp. 251–258.
Tonyé, E., Akono, A., 2002. Two approaches of textural classification for the location of the flows of lava on the volcanic site of the mountain Cameroon. Geocarto International 17 (4), 35–46.
Valade, S., Lacanna, G., Coppola, D., Laiolo, M., Pistolesi, M., Delle Donne, D., Genco, R., Marchetti, E., Ulivieri, G., Allocca, C., Cigolini, C., Nishimura, T., Poggi, P., Ripepe, M., 2016. Tracking dynamics of magma migration in open-conduit systems. Bull. Volcanol. 78 (11), 78.
Wadge, G., Haynes, M., 1998. Cover radar images growth of Soufriere Hills volcano, Montserrat. Int. J. Remote Sens. 19, 797–800.
Wadge, G., Scheuchl, B., Stevens, N.F., 2002. Spaceborne radar measurements of the eruption of Soufriere Hills volcano, Montserrat. Geological Society, London, Memoirs 21 (1), 583–594.
Wadge, G., Macfarlane, D.G., Robertson, D.A., Hale, A.J., Pinkerton, H., Burrell, R.V., Norton, G.E., James, M.R., 2005. AVTIS: a novel millimetre-wave ground based instrument for volcano remote sensing. J. Volcanol. Geotherm. Res. 146 (4), 307–318.
Wadge, G., Cole, P., Stinton, A., Komorowski, J.C., Stewart, R., Toombs, A.C., Legendre, Y., 2011. Rapid topographic change measured by high-resolution satellite radar at Soufriere Hills volcano, Montserrat, 2008–2010. J. Volcanol. Geotherm. Res. 199 (1), 142–152.
Wadge, G., Macfarlane, D.G., Odbert, H.M., James, M.R., Hole, J.K., Ryan, G., Bass, V., De Angelis, S., Pinkerton, H., Robertson, D.A., Loughlin, S.C., 2008. Lava dome growth and mass wasting measured by a time series of ground-based radar and seismicity observations. J. Geophys. Res. Solid Earth 113 (8), B08210.
Wadge, G., Voight, B., Sparks, R.S.J., Cole, P.D., Loughlin, S.C., Robertson, R.E.A., 2014. An overview of the eruption of Soufriere Hills Volcano, Montserrat from 2000 to 2010. Geol. Soc. Lond. Mem. 39 (1), 1–40.
Walter, T.R., Subandriyo, J., Kirbani, S., Bathke, H., Suryanto, W., Aisyah, N., Dahm, T., 2015. Volcano-tectonic control of Merapi's lava dome splitting: the November 2013 fracture observed from high resolution TerraSAR-X data. Tectonophysics 639, 23–33.
Whelley, P.L., Glaze, L.S., Calder, E.S., Harding, D.J., 2014. LiDAR-derived surface roughness texture mapping: application to Mount St. Helens pumice plain deposit analysis. IEEE Trans. Geosci. Remote Sens. 52 (1), 426–438.
Wittmann, W., Sigmundsson, F., Dumont, S., Lavallée, Y., 2017. Post-emplacement cooling and contraction of lava flows: InSAR observations and a thermal model for lava fields at Hekla volcano, Iceland. J. Geophys. Res. Solid Earth 122 (2), 946–965.
Zakšek, K., Hort, M., Lorenz, E., 2015. Satellite and ground based thermal observation of the 2014 effusive eruption at Stromboli Volcano. Remote Sens. 7 (12), 17190–17211.
Zebker, H.A., Rosen, P., Hensley, S., Mouginis-Mark, P.J., 1996. Analysis of active lava flows on Kilauea volcano, Hawaii, using SIR-C radar correlation measurements. Geology 24 (6), 495–498.
Zebker, H.A., Rosen, P.A., Hensley, S., 1997. Atmospheric effects in interferometric synthetic aperture radar surface deformation and topographic maps. J. Geophys. Res. Solid Earth 102 (B4), 7547–7563.